Journal of Non-Newtonian Fluid Mechanics 333 (2024) 105307

Contents lists available at ScienceDirect

Journal of Non-Newtonian Fluid Mechanics

journal homepage: www.elsevier.com/locate/jnnfm

Full length article

σOWCh: Optimally Windowed Chirp rheometry using combined motor transducer/single head rheometers

Rebecca E. Hudson-Kershaw [a], Mohua Das [b], Gareth H. McKinley [b,a], Daniel J. Curtis [a,*]

[a] Complex Fluids Research Group, Department of Chemical Engineering, Swansea University, Fabian Way, Swansea, SA1 8EN, Swansea, UK
[b] Department of Mechanical Engineering, Massachusetts Institute of Technology, MA 02139, Cambridge, USA

ARTICLE INFO

Keywords:
Optimally Windowed Chirp rheometry
Linear viscoelasticity
Rheometry
Experimental techniques

ABSTRACT

Recent advances in rheometry exploiting frequency-modulated (chirp) waveforms have dramatically reduced the time required to perform linear viscoelastic characterisation of complex materials. However, the technique was optimised for 'separate motor transducer' instruments, in which the drive motor imposing the strain deformation is decoupled from the torque transducer. Whilst the use of optimised windowed chirps (OWCh) using other rheometers has been recently reported in the literature, no systematic study concerning the use of 'combined motor transducer' instruments (in which the motor and transducer subsystems are integrated into a single 'head') has been undertaken. In the present study, we demonstrate the use of OWCh rheometry using combined motor transducer/single-head rheometers using a stress-controlled operating principle, thus avoiding the reliance on complicated and instrument-specific feedback control systems that would be required to perform strain-controlled experiments. The use of stress-controlled chirps requires a modification to the established OWCh analysis protocol such that the complex viscosity $\eta^*(\omega)$ is used as an intermediate proxy function for ultimately computing the complex modulus $G^*(\omega)$. This approach negates the effect of the strain offset that is inherent to stress-controlled oscillatory rheometry. Secondly, a correction algorithm and operational criteria for identifying inertial artefacts is established before we consider the impact of chirp digitisation on data acquisition. The use of stress-controlled OWCh rheometry (which we term Stress-OWCh, i.e. σOWCh) is demonstrated for a diverse range of material classes including, Newtonian calibration fluids (silicone oil), polymer solutions (polyethylene oxide in water), an entangled polymer melt (polydimethylsiloxane), worm-like micellar systems (cetylpyridinium chloride/sodium salicylate), time-evolving critical gels (gelatin) and aging elastoviscoplastic materials (Laponite®). This novel implementation of chirp waveforms using a single-head rheometer will facilitate the wider adoption of OWCh rheometry and allow the benefits of frequency-modulation techniques to be exploited where separate motor transducer instruments are unavailable/unsuitable.

1. Introduction

Linear viscoelastic characterisation of complex fluids and soft solids is perhaps the most common rheometric operation and allows the molecular architecture and relaxation dynamics of a sample, that is often (but not exclusively) polymeric in nature, to be investigated. Experiments can be designed to monitor the transient evolution of these properties with time/extent of reaction and other environmental parameters such as temperature and pH. The data obtained from linear viscoelastic property measurement also provide a basis for quality control/quality assurance (QC/QA) assays, often in conjunction with the determination of the steady-state flow curve of the material. Conventional linear viscoelastic characterisation is often performed in the frequency domain by considering the mechanical response of a material to a discrete sequence of small amplitude, single-tone, oscillations. However, this frequency sweep (FS) approach is time consuming and can be the source of QA/QC bottlenecks. Further, when probing microstructural evolution (e.g. gelation/curing) [1–4] using repeated FS experiments, the evolving rheological properties, compete with the constraint that the material be assumed to be *linear time invariant* (LTI) during each frequency sweep. This limits the duration, and hence frequency content of the FS signal. A useful alternative to the FS is the multi-wave experiment (often termed Fourier Transform Mechanical Spectroscopy, FTMS) in which the material is probed at multiple frequencies simultaneously using a composite waveform constructed from a fundamental base frequency and several harmonics [5,6]. Whilst FTMS experiments allow the linear viscoelastic properties of the material to be assessed rapidly, the deformation associated with each

* Corresponding author.
E-mail address: d.j.curtis@swansea.ac.uk (D.J. Curtis).

https://doi.org/10.1016/j.jnnfm.2024.105307
Received 20 June 2024; Received in revised form 23 August 2024; Accepted 24 August 2024
Available online 30 August 2024

component frequency contributes to the total strain amplitude, which must remain within the linear viscoelastic range of the material, hence the amplitude of each component frequency must be reduced compared to the FS approach.

The use of broadband experimental techniques in the rapid linear viscoelastic characterisation of complex fluids is gaining popularity [7–11]. Such techniques allow the linear viscoelastic parameters characterising an unknown material (such as time-evolving complex modulus of an aging or mutating material, $G^*(\omega, t_w)$) to be determined, with very high frequency resolution, in a fraction of the time required by conventional FS based rheometric protocols. One such technique uses frequency modulated 'Chirp signals' [7,12–15] which, whilst exploited in acoustics [16] and radar [17] for many years, have only recently been used for complex fluids characterisation. A chirp waveform, in which the frequency evolves from ω_1 to ω_2 over the waveform duration T (in this case exponentially) can be mathematically expressed as follows:

$$x(t) = x_0 \sin\left(k_1[e^{k_2 t} - 1]\right) \tag{1}$$

where $k_1 = \omega_1 T / \log(\omega_2/\omega_1)$ and $k_2 = \log(\omega_2/\omega_1)/T$. Hence, the instantaneous frequency evolves as:

$$\omega(t) = \omega_1 \left(\frac{\omega_2}{\omega_1}\right)^{t/T} \tag{2}$$

and all frequencies $\omega_1 \leq \omega \leq \omega_2$ are probed by the waveform. As such, the signals are ideally suited to probing the transfer function of LTI material systems. In terms of mechanical analysis, one may probe the complex modulus $G^*(\omega)$ by defining this as the transfer function between an applied perturbation (strain, γ) and the response of the material in terms of stress (σ), i.e.:

$$G^*(\omega) = \frac{\mathcal{F}[\sigma]}{\mathcal{F}[\gamma]} \tag{3}$$

where $\mathcal{F}(.)$ denotes the Fourier Transform.

However, analysis of a waveform such as (Eq. (1)) using a Discrete Fourier Transform results in the convolution of the Fourier transform of the material response to the perturbation waveform itself and the Fourier transform of a rectangular signal envelope. This leads to the generation of sidelobes and 'spectral leakage' (i.e. the loss of information from the frequency spectrum between ω_1 and ω_2), thus preventing accurate determination of the desired linear response function, i.e. $G^*(\omega)$. Further, the absence of periodicity in the waveforms may exacerbate spectral leakage. Geri et al. [7] demonstrated that such issues can be effectively minimised by (i) ensuring that the Time-Bandwidth product of the forcing signal, $\mathrm{TB} = T(\omega_2 - \omega_1)/2\pi$, is large and (ii) multiplying the chirp signal with a Tukey style windowing function, which ensures periodicity in both the imposed perturbation and material response waveforms (since the Tukey window smoothly grows from, and returns to, zero at $t = 0$ and $t = T$, respectively) thus minimising spectral leakage. The corresponding forcing function is thus [7]:

$$x(t) = x_0 \begin{cases} \cos^2\left[\frac{\pi}{r}\left(\frac{t}{T} - \frac{r}{2}\right)\right] \sin\left(k_1[e^{k_2 t} - 1]\right), & \frac{t}{T} \leq \frac{r}{2} \\ \sin\left(k_1[e^{k_2 t} - 1]\right), & \frac{r}{2} < \frac{t}{T} < 1 - \frac{r}{2} \\ \cos^2\left[\frac{\pi}{r}\left(\frac{t}{T} - 1 + \frac{r}{2}\right)\right] \sin\left(k_1[e^{k_2 t} - 1]\right), & \frac{t}{T} \geq 1 - \frac{r}{2} \end{cases} \tag{4}$$

where r denotes a windowing parameter which defines the steepness of the window function as $t \to 0$ and $t \to T$. An Optimally Windowed Chirp (OWCh) waveform that permitted $G^*(\omega)$ to be determined accurately over a wide frequency range was proposed with $r = 0.1$. Fig. 1 compares, for illustrative purpose, the unwindowed and windowed ($r = 0.5$) signals.

Chirp-based protocols are particularly useful in the study of mutating materials [7,14] since a wide frequency band can be excited in a relatively short experiment, allowing the evolution of the frequency-dependent viscoelastic properties of a sample to be monitored using a sequence of chirps (the material being assumed to be an LTI system locally during each chirp). In the context of gelling samples, for example, such data allows the gel point (GP), which identifies the transition from viscoelastic liquid to viscoelastic solid, to be determined [1,2,5,6,18]. However, the ability to rapidly acquire viscoelastic spectra finds more general use in the efficient and high throughput characterisation of a wide variety of samples. The present work focusses on linear viscoelastic characterisation but the use of chirp protocols in the non-linear regime has been demonstrated, through the use of orthogonal superposition, by Rathinaraj et al. [19]. In addition it is possible to consider future combinations of chirp protocols and slowly swept strain (or stress) amplitude-modulated approaches using for example the Gaborheometry approach [20].

Whilst OWCh protocols can be implemented using a TA Instruments ARES-G2 rheometer following Geri et al. [7] or the Anton Paar MCR702 (Twin Drive) following Athanasiou et al. [15], both of which operate as Separate Motor Transducer (SMT) devices, implementing such protocols using Combined Motor Transducer (CMT) instruments can be challenging. Whilst modern CMT rheometers are often able to perform strain-controlled experiments requiring steady unidirectional shear or steady state oscillatory waveforms exceptionally well (as discussed by Lauger [21]), it can be difficult for the rheometer to achieve a desired chirp waveform since the frequency and phase of the applied deformation wave (and also the response of the material to that deformation) is evolving dynamically throughout the duration of waveform. The nonlinear feedback and control algorithms have also been optimised for single frequency periodic oscillatory deformations. Modern CMT rheometers utilise either Drag Cup or Electrically Commutated motor technology, both of which work on the principle that the achieved torque (and thus the stress applied to the sample) is proportional to the current applied to the motor, and a more effective approach may be to invoke the torque-controlled operation mode of the CMT rheometer to apply stress-controlled and frequency-modulated signals such as a chirp.

In addition to avoiding the need for strain-controlled feedback loops, the use of stress-controlled chirps has other benefits. For example, in gelling materials, it is necessary to balance the limited linear viscoelastic range (LVR) of the post-gel point regime with achieving sufficient resolution of the response waveform in the pre-gel regime. Strain-controlled protocols typically sacrifice pre-GP stress resolution to ensure that the strain at (and beyond) the GP remains within the LVR [7,12–14]. Employing a stress-controlled protocol allows good data to be obtained throughout the gelation process since the strain amplitude attained naturally decreases as the relaxation spectrum of the material (and hence the zero shear viscosity) evolves towards the GP [4]. Materials characterised by a limited and frequency-dependent LVR may also benefit from the use of stress-controlled, chirp-based rheometry. When employing a strain-based chirp protocol on such materials, the strain amplitude will be limited by the extent of the high-frequency LVR which, at low frequencies, may be insufficient to generate a resolvable torque signal. The response of such a material to a stress-based chirp (with the stress amplitude determined based on both high and low-frequency LVR considerations) would be characterised by larger strains at low frequencies thus allowing good resolution to be achieved across a far wider frequency range. Stress-controlled experiments are often also employed in studies of yield stress fluids [20]. By applying stress amplitudes that are either below or above the critical flow stress the evolution of the frequency-dependent properties of an elastoviscoplastic material can be followed as the material yields and begins to flow. Finally, the ability to perform chirp-based rheometry on Combined Motor Transducer (CMT) rheometers (also often referred to as single head (SH) rheometers) will facilitate the wider adoption of OWCh and allow its benefits to be exploited where native strain-controlled instruments are unavailable, as most instruments in non-specialist/industrial laboratories are CMT units.

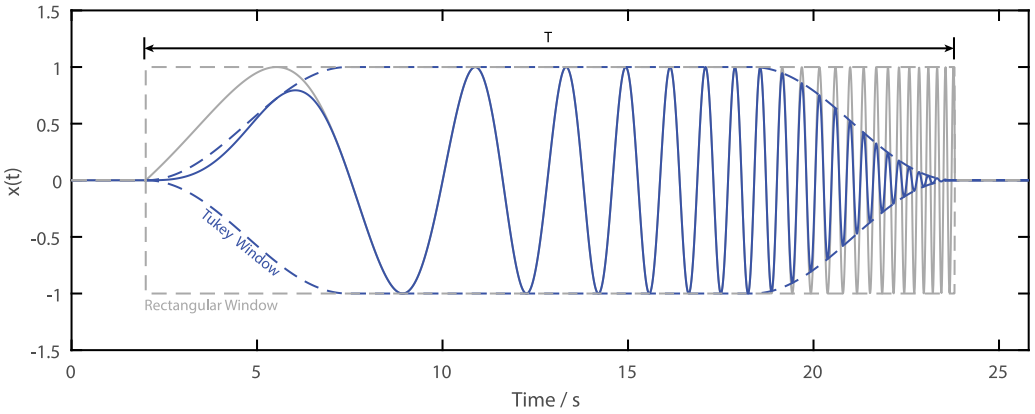

Fig. 1. Comparison of un-windowed chirp (grey) and Tukey windowed chirp (blue) waveforms. Dashed lines show the signal envelopes (i.e. window functions). Note that the optimum windowed chirp was found to be $r = 0.1$ in Geri et al. [7], but a waveform with $r = 0.5$ is shown here for clarity.

The response of most samples to stress-controlled (single-tone) oscillations does not result in a strain waveform that oscillates around zero strain; a constant 'strain offset' is observed which can be used to probe the zero shear viscosity as recently demonstrated experimentally by Lee et al. [22] and analytically by Hassager [23] and Ogunkeye et al. [24]. In Section 2.1 we extend the modelling of Hassager (for single-tone oscillations) to the stress-controlled chirp and demonstrate that, for such perturbations, the offset evolves throughout the chirp waveform. The presence of this time varying offset is problematic in terms of extracting the complex modulus from the σOWCh experiment since, whilst the driving stress waveform is periodic, the strain response is not and subsequent Fourier Transformation of the data generates significant Fresnel ripples in the computed moduli which render the results unusable (the time dependency of the offset preventing it from appearing as a simple DC term in the FFT). Herein, we propose to overcome this issue by performing Fourier analysis on the time derivative of the strain data (i.e. the strain rate) and seeking the complex viscosity, $\eta^*(\omega)$, before converting this to the complex modulus through the well-known relation $G^*(\omega) = i\omega\eta^*(\omega)$. Notably, a recent study of the aging of Bentonite samples using chirp-based rheometry was performed using a TA Instruments DHR3 rheometer (a CMT device) operated in its stress-controlled mode (thus avoiding the need to employ feedback loops) in which $G^*(\omega)$ was determined from the stress and strain waveforms directly [20]. However, the Bentonite sample displayed a yield stress thus driving the strain offset to zero. Other classes of materials, which do not display a yield stress cannot be analysed accurately using FFT analysis of the stress and strain waveforms.

In addition to the issues associated with the evolving strain offset, experiments performed on CMT rheometers are subject to the effects of both 'instrument' and 'sample' inertia. In contrast to SMT rheometers, for which torque is measured at the stationary part of the geometry, in CMT rheometers torque application and displacement measurement both occur at the moving element of the geometry. As such, some of the applied torque must be used to accelerate the moving parts of the rheometer (motor, shaft and geometry). Such 'instrument' inertial effects have been discussed in detail by several authors [24–31], including Prof. Ken Walters in his 1975 book 'Rheometry' [32], and it is well understood that inertial artefacts can (i) introduce a quadratic scaling with $G'(\omega) \sim I\omega^2$ at high frequencies and (ii) generate a resonant coupling between the instrument and the sample elasticity which dramatically reduces the torque amplitude applied to the material at high frequencies. Ogunkeye, Hudson & Curtis [24] recently evaluated the impact of inertia on the start up of stress-controlled oscillations following the analysis of Hassager [23] for the inertialess case. In Section 2.2 we extend this analysis to study the impact of instrument inertia on the response of the combined system (i.e. the rheometer and the loaded material sample) to a σOWCh perturbation and demonstrate that understanding its effects are critical to performing accurate chirp-based rheometry using CMT rheometers.

In Section 2.3 we consider the implications of waveform digitisation. This discretisation process occurs within the rheometer software and results in the generation of a look up table (LUT) that is sent to the rheometer as a command signal. The chirp signal is reconstructed by the rheometer hardware using an interpolation function to generate the perturbation waveform. This operation generates limitations on the range of waveform parameters and we present guidelines for OWCh waveform design based on the size of the LUT (which can differ dramatically between rheometer models) and the frequency range it is desired to study.

In Section 3 we demonstrate the use of the σOWCh on a wide range of model systems; (i) a silicone oil (ii) a polydimethylsiloxane (PDMS) which we consider as a room temperature entangled polymer melt, (iii) a polymer solution (polyethyleneoxide) (iv) a worm-like micellar system, (v) a gelatin sample undergoing gelation, and finally (vi) Laponite® (an aging, yield stress material).

2. Modelling

2.1. Strain offset

We begin by considering the response of a general viscoelastic material to a σOWCh perturbation following Hassager (2020) [23] who, working in the Laplace domain, derived an analytical expression for the strain response to the start-up of a (single-tone) stress-controlled oscillatory perturbation. However, the Laplace transform of the chirp signal cannot be computed easily and hence we consider an arbitrary waveform constructed as a piecewise function of N steps, each having discrete frequency ω_i initiated at time t_i and terminating at t_{i+1}. The chirp function can then be approximated by discretising ω and t (as per Eq. (2)). The stress profile for this arbitrary waveform can then be expressed as:

$$\sigma = \sigma_0 \sum_{i=1}^{N-1} \left[H(t-t_i)\sin(\omega_i(t-t_i)+\phi_i) - H(t-t_{i+1}) \times \sin(\omega_i(t-t_{i+1})+\phi_{i+1}) \right] \tag{5}$$

where $H(t-t_i)$ denotes the Heaviside step function and

$$\phi_i = \sum_{j=1}^{i-1} \omega_j (t_j - t_{j-1}) \tag{6}$$

expresses the accumulated phase of the perturbation waveform up to t_i.

Noting that the Boltzmann superposition principle expresses the stress at the present time, $\sigma(t)$, as a convolution of the stress relaxation modulus, $G(t-t')$ and the deformation history $\dot{\gamma}(t')$,

$$\sigma = \int_{-\infty}^{t} G(t-t')\dot{\gamma}(t')dt' \tag{7}$$

in the Laplace domain one can write:

$$y(s) = \frac{1}{s}\dot{y}(s) = \frac{1}{s}\frac{x(s)}{g(s)} \tag{8}$$

where $y(s)$, $\dot{y}(s)$, $x(s)$ and $g(s)$ denote the Laplace transforms of $\gamma(t)$, $\dot{\gamma}(t)$, $\sigma(t)$ and $G(t)$, respectively. Whilst the proposed data processing algorithm employs $\dot{\gamma}(t)$ which could be determined analytically as $\mathscr{L}^{-1}\left[x(s)/g(s)\right]$, the rheometer does not directly record this function for arbitrary waveforms and $\dot{\gamma}(t)$ must be determined numerically. Hence, in the present section, we seek to determine $\gamma(t)$. Noting that $t_i = t_{i+1} - (t_{i+1} - t_i)$, the Laplace transform of $\sigma(t)$ can be determined from Eq. (5) as:

$$x(s) = \sigma_0 \sum_i \left\{ e^{-t_i s}\left[\frac{s\sin(\phi_i) + \omega_i\cos(\phi_i)}{(s^2+\omega_i^2)}\right] - e^{-st_{i+1}}\left[\frac{s\sin(\phi_{i+1}) + \omega_i\cos(\phi_{i+1})}{(s^2+\omega_i^2)}\right]\right\} \tag{9}$$

By substituting Eq. (9) into Eq. (8) we arrive at the following expression for $y(s)$:

$$y(s) = \sigma_0 \sum_i \left\{ e^{-t_i s}\left[\frac{s\sin(\phi_i) + \omega_i\cos(\phi_i)}{s(s^2+\omega_i^2)g(s)}\right] - e^{-st_{i+1}}\left[\frac{s\sin(\phi_{i+1}) + \omega_i\cos(\phi_{i+1})}{s(s^2+\omega_i^2)g(s)}\right]\right\} \tag{10}$$

The time domain function $\gamma(t)$ can now be determined by taking the inverse Laplace transform of Eq. (10) by considering its poles.

Firstly, we note that:

$$\mathscr{L}^{-1}\left[e^{-as}F(s)\right] = H(t-a)f(t-a) \tag{11}$$

such that we can write:

$$\gamma(t) = \sigma_0 \sum_i \left\{ H(t-t_i)\mathscr{L}^{-1}\left[\frac{s\sin(\phi_i) + \omega_i\cos(\phi_i)}{s(s^2+\omega_i^2)g(s)}\right]_{(t-t_i)} - H(t-t_{i+1})\mathscr{L}^{-1}\left[\frac{s\sin(\phi_{i+1}) + \omega_i\cos(\phi_{i+1})}{s(s^2+\omega_i^2)g(s)}\right]_{(t-t_{i+1})}\right\} \tag{12}$$

where the notation $\mathscr{L}^{-1}\left[F(s)\right]_{(t-t_i)}$ denotes that the variable of the time domain function, f, will be shifted by a constant t_i. For later use, we note that the arguments of both inverse Laplace transforms in Eq. (12) have the same form:

$$B(s) = \frac{s\sin a + \omega_i\cos a}{s(s^2+\omega_i^2)g(s)} \tag{13}$$

Each of the inverse Laplace transform terms in Eq. (12) will have poles at $s = 0$ (corresponding to the long time behaviour of the system, i.e. the offset), at $s = \pm i\omega_i$ (corresponding to the periodic response) and where s generates zeros of $g(s)$ (corresponding to the transient response of the material to the frequency steps). We now treat each of these poles separately. Firstly, the contribution to $\gamma(t)$ from the pole at $s = 0$ can be determined by noting that $g(0) = \eta_0$ and applying the final value theorem,

$$\lim_{t\to\infty} f(t) = \lim_{s\to 0} sF(s) \tag{14}$$

such that:

$$\gamma_{off}(t) = \sigma_0 \sum_i \left[\frac{H(t-t_i)\cos(\phi_i)}{\omega_i\eta_0} - \frac{H(t-t_{i+1})\cos(\phi_{i+1})}{\omega_i\eta_0}\right] \tag{15}$$

We now consider the periodic contribution to the signal ($s = \pm i\omega_i$), evaluating $f(s) = (\omega^2 + s^2)B(s)$ at the point $s = i\omega$ we find,

$$f(s) = \frac{i\omega_i\sin a + \omega_i\cos a}{i\omega_i g(i\omega_i)} \tag{16}$$

Recalling that,

$$G^*(\omega) = i\omega\int_0^\infty G(t)e^{-i\omega t}dt = i\omega g(i\omega) \tag{17}$$

we can write that

$$g(i\omega) = \frac{G^*(\omega)}{i\omega} \tag{18}$$

and since $J^* = 1/G^*$

$$J^*(\omega) = \frac{1}{i\omega g(i\omega)} \tag{19}$$

hence,

$$f(i\omega_i) = J^*\left(i\omega_i\sin a + \omega_i\cos a\right) = \left(J' - iJ''\right)\left(i\omega_i\sin a + \omega_i\cos a\right) \tag{20}$$

which has real (f_r) and imaginary (f_i) parts given by

$$f_r = \omega(J'\cos a + J''\sin a) \tag{21}$$

$$f_i = \omega(J'\sin a - J''\cos a) \tag{22}$$

The combined contribution from $s = \pm i\omega_i$ is then:

$$b_p(t) = J'\sin(a+\omega_i t) - J''\cos(a+\omega_i t) \tag{23}$$

Introducing Eq. (23) into Eq. (10) we find that the periodic contribution to $\gamma(t)$ is:

$$\gamma_p(t) = \sigma_0 \sum_i \left\{ H(t-t_i)\left[J_i'\sin(\phi_i + \omega_i(t-t_i)) - J_i''\cos(\phi_i + \omega_i(t-t_i))\right] - H(t-t_{i+1})\left[J_i'\sin(\phi_{i+1} + \omega_i(t-t_{i+1})) - J_i''\cos(\phi_{i+1} + \omega_i(t-t_{i+1}))\right]\right\} \tag{24}$$

where the subscript p denotes the 'periodic' part of the material response whilst J_i' and J_i'' denote the real and imaginary parts of the complex compliance evaluated at ω_i.

Finally, the transient contribution to $\gamma(t)$ needs to be considered. Again following Hassager [23], we consider a multi-mode Maxwell model with N_m relaxation times τ_m and associated viscosities η_m such that:

$$g(s) = \sum_m \frac{\eta_m}{1+s\tau_m} \tag{25}$$

This function will have singularities at $s = -1/\tau_m$. Outside of these singularities

$$\frac{dg}{ds} = -\sum_m \frac{\eta_m\tau_m}{(1+s\tau_m)^2} < 0 \tag{26}$$

and hence a single root, s_1, of $g(s) = 0$ is found in each of the intervals

$$-\frac{1}{\tau_m} < s < -\frac{1}{\tau_{m+1}} \tag{27}$$

which can be used to define (following Hassager [23]) $N_k = N_m - 1$ positive retardation times λ_k such that:

$$\tau_m < \lambda_k < \tau_{m+1} \tag{28}$$

(Note that a single-mode Maxwell model has no retardation time).

The total contribution of the poles at s_k to $B(s)$ can be determined by summing the residues of $B(s)\exp(-st)$ at the poles [33]. Close to a given pole (of $B(s)$), by definition $g(-1/\lambda_k) = 0$ and hence, $g(s)$ can be expanded as:

$$g(s) = \left(s + \frac{1}{\lambda_k}\right)g'\left(-\frac{1}{\lambda_k}\right) + O(s^2) \tag{29}$$

Hence, to first order, we have:

$$g(s) = -\lambda_k^2 \left(s + \frac{1}{\lambda_k} \right) \sum_m \frac{\eta_m \tau_m}{(\lambda_k - \tau_m)^2} \tag{30}$$

(note that higher order terms of Eq. (29) will not contribute to the residual since the term $(s+1/\lambda_k)^n \to 0$ as $s \to -1/\lambda_k$). We now substitute this into Eq. (13), multiply by e^{st} and take the residue of the pole occurring at $-1/\lambda_k$ to get:

$$\text{Res}\left[B(s)e^{st}, -\frac{1}{\lambda_k} \right] = \frac{\left[\omega\lambda_k \cos a - \sin a\right] e^{-t/\lambda_k}}{(1+\omega^2\lambda_k^2)\sum_m \frac{\eta_m\tau_m}{(\lambda_k-\tau_m)^2}} \tag{31}$$

Summing over all roots (one of which appears between each pair of relaxation times) and substituting into Eq. (10) allows the transient contribution to the strain to be determined as:

$$\gamma_t(t) = \sigma_0 \sum_i \left\{ H(t-t_i) \sum_k \frac{\left[\omega_i\lambda_k \cos\phi_i - \sin\phi_i\right] e^{-(t-t_i)/\lambda_k}}{(1+\omega_i^2\lambda_k^2)\sum_m \frac{\eta_m\tau_m}{(\lambda_k-\tau_m)^2}} \right.$$
$$\left. - H(t-t_{i+1}) \sum_k \frac{\left[\omega_i\lambda_k \cos\phi_{i+1} - \sin\phi_{i+1}\right] e^{-(t-t_{i+1})/\lambda_k}}{(1+\omega_i^2\lambda_k^2)\sum_m \frac{\eta_m\tau_m}{(\lambda_k-\tau_m)^2}} \right\} \tag{32}$$

Hence, (neglecting inertia) the total strain as a function of time can be written as:

$$\gamma(t) = \gamma_{off}(t) + \gamma_p(t) + \gamma_t(t) \tag{33}$$

2.1.1. The windowed chirp signal

For a windowed chirp (i.e. an OWCh experimental protocol) the parameter σ_0 in Eq. (5) becomes a time-dependent variable, however, within each discrete interval of Eq. (5), $\sigma_0(t_i)$ takes a constant value (which changes between intervals) and hence the windowed chirp can be accommodated by discretising σ_0 in the same manner as ω and t.

2.1.2. Two mode Maxwell model

A two-mode Maxwell model represents the simplest mechanical model with a retardation time (and hence involves a transient contribution to the total strain). The retardation time, λ, for a two-mode Maxwell model (with relaxation times τ_1, τ_2 and mode viscosities of η_1 and η_2) can be expressed as:

$$\lambda = \frac{\eta_1\tau_2 + \eta_2\tau_1}{\eta_1 + \eta_2} \tag{34}$$

whilst

$$J'(\omega) = \frac{\eta_1\tau_1 + \eta_2\tau_2 + (\eta_1\tau_2 + \eta_2\tau_1)\tau_1\tau_2\omega^2}{(\eta_1+\eta_2)^2 + (\eta_1\tau_2 + \eta_2\tau_1)^2\omega^2} \tag{35}$$

$$J''(\omega) = \frac{\eta_1 + \eta_2 + (\eta_1\tau_2^2 + \eta_2\tau_1^2)\omega^2}{\omega(\eta_1+\eta_2)^2 + (\eta_1\tau_2 + \eta_2\tau_1)^2\omega^3} \tag{36}$$

$$\eta_0 = \eta_1 + \eta_2 \tag{37}$$

Eqs. (34) through (37) can be combined with Eqs. (5) and (33) to determine the strain response (in the absence of instrument/sample inertia effects) of a two-mode Maxwell model to a given windowed chirp. Fig. 2 shows the response of a two-mode Maxwell model with $\tau_1 = 0.1$ s, $\tau_2 = 1$ s and $\eta_1 = \eta_2 = 1.0$ Pa s to a stress-controlled OWCh waveform which clearly shows that a strain offset is a key feature of the response. Consequently, if the conventional OWCh protocol, which calculates the dynamic moduli via

$$G^*(\omega) = \frac{\mathcal{F}[\sigma]}{\mathcal{F}[\gamma]} \tag{38}$$

is used to process the waveforms, the resulting moduli show no resemblance to the expected result (Fig. 2D). However, provided the bandwidth of the chirp is sufficiently wide (approximately 2 orders of magnitude) this offset term approaches a constant in the latter half of the experiment (see Fig. 2B) and the expected moduli may be recovered via:

$$G^*(\omega) = i\omega\eta^*(\omega) = \frac{i\omega\mathcal{F}[\sigma]}{\mathcal{F}[\dot{\gamma}]} \tag{39}$$

as shown in Fig. 2E.

Note that if one seeks $\dot{\gamma}(t)$ rather than $\gamma(t)$ in the analysis above, the final value theorem reveals that $\dot{\gamma}(\infty) = 0$ confirming the absence of the offset and the validity of seeking $\eta^*(\omega)$ as an intermediate to obtaining $G^*(\omega)$.

This approach requires that the derivative of the strain signal be obtained. In the present work a second order central difference approach has been used to determine $\dot{\gamma}$ (for data points $i = 2 : N-1$, whilst for $i = 1$ and $i = N$ first order forward/backward differences are employed, respectively). Whilst this operation exacerbates noise, this is typically only important at a higher frequency than ω_2 and hence does not impede the determination of $G^*(\omega)$ over the range $\omega_1 \le \omega \le \omega_2$.

In a similar fashion, whilst direct calculation of the complex compliance, $J^*(\omega)$ as

$$J^*(\omega) = \frac{FFT(\gamma)}{FFT(\sigma)} \tag{40}$$

results in significant noise, the material function can be obtained via a complex fluidity, $\Phi^*(\omega) = \Phi' - i\Phi''$ (the negative imaginary part being required to ensure positive values of J' and J'') as:

$$J^*(\omega) = \frac{\Phi^*(\omega)}{i\omega} \tag{41}$$

where

$$\Phi^*(\omega) = \frac{FFT(\dot{\gamma})}{FFT(\sigma)} \tag{42}$$

In the present work we choose to work with the complex viscosity and complex modulus $G^*(\omega)$ (rather than reporting the complex compliance $J^*(\omega)$) due to their predominance in the literature, and to facilitate ready comparison with previous work using strain-controlled chirps.

2.2. Inertia

Having demonstrated that $G'(\omega)$ and $G''(\omega)$ can be accurately determined from a σOWCh experiment if one seeks $\eta^*(\omega)$ as an intermediate parameter, we now consider the impact of instrument inertia on the strain waveform.

Unlike SMT instruments, in which the torque-sensing element of the geometry is separated from that which is driven by the motor, in CMT rheometers the application of torque and displacement sensing both occur at the moving element of the geometry (which is undergoing continuous acceleration in oscillatory flows). Hence, both the sample and instrument inertia contribute to the total stress recorded by the instrument. In the limit of 'gap loading', where sample inertia is deemed to be negligible [34], the total torque (M_t) can be expressed as the sum of the sample torque, M_s and the inertial torque as follows:

$$M_t = M_s + I_c\ddot{\theta} \tag{43}$$

where I_c is the calibrated moment of inertia constant of the system (i.e. including instrument and geometry components) and $\theta(t)$ denotes the instantaneous angular displacement. Consequently, in the presence of inertia, Eq. (7) becomes:

$$\sigma_t(t) = \int_{-\infty}^{t} G(t-t')\dot{\gamma}(t')dt' + I\ddot{\gamma} \tag{44}$$

where σ_t denotes the total stress ($= M_t/K_\sigma$). Note that $I = I_c(K_\sigma/K_\gamma)$ where K_σ and K_γ denote the geometry-specific stress and strain factors, respectively. Hence the Laplace domain function becomes

$$y(s) = \frac{1}{s}\frac{x(s)}{g(s) + Is} \tag{45}$$

Ogunkeye, Hudson & Curtis [24] demonstrated that, for single-tone oscillations, the additional term (Is) in the denominator of Eq. (45)

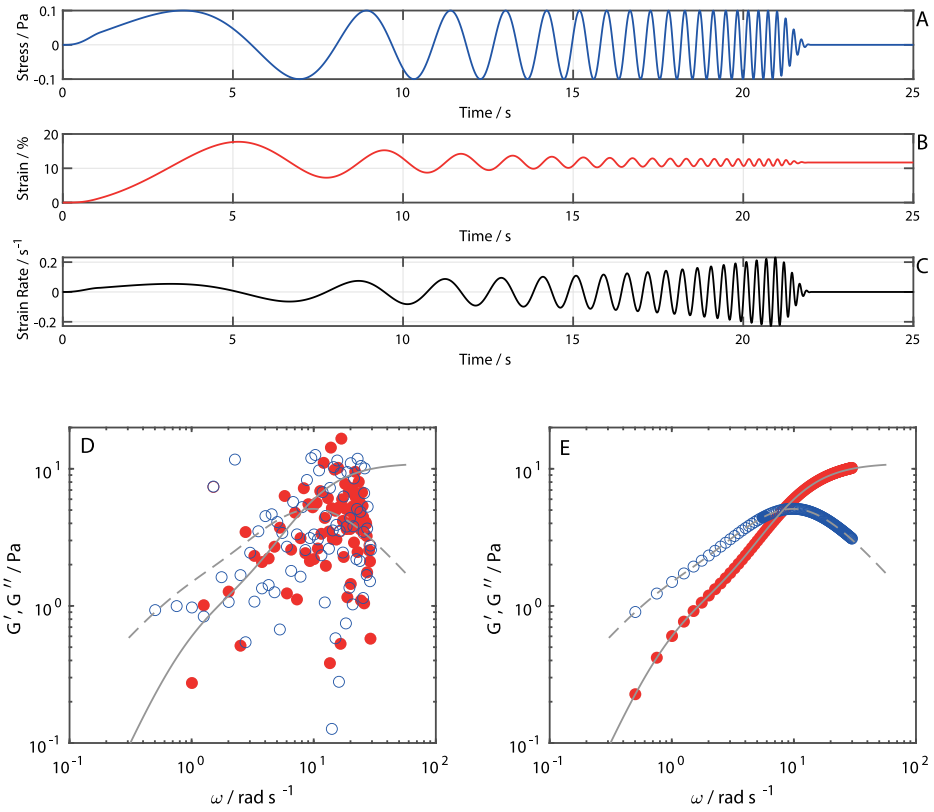

Fig. 2. Perturbation (A) and response (B&C) for a two-mode Maxwell model (Eq. (33)) with $\tau_1 = 0.1$ s, $\tau_2 = 1$ s and $\eta_1 = \eta_2 = 1.0$ Pa s. Calculating $G^*(\omega)$ as using the standard OWCh protocol, based on the FFT of the stress and strain waveforms, generates very poor data (D) due to the offset observed in the strain profile (B). Calculating $G^*(\omega)$ based on the FFT of the stress and strain-rate waveforms, generates storage (closed red) and loss (open blue) moduli that are in excellent agreement with their SAOS counterparts (solid grey and dashed grey lines, respectively)(E).

impacts the form of both the transient and periodic contributions to $\gamma(t)$. For non-zero values of I, the periodic part of the strain (for a single-tone stress controlled excitation) can be expressed as [24]:

$$\gamma_p(t) = \frac{\sigma_0 \left[\left(G' - I\omega^2\right)\sin(\psi + \omega t) - G''\cos(\psi + \omega t)\right]}{\left(G' - I\omega^2\right)^2 + G''^2} \tag{46}$$

In contrast to the inertialess case, for which the transient response associated with each pair of relaxation modes is defined by a single root of the function $g(s) = 0$ in the interval $-1/\tau_m < s_k < -1/\tau_{m+1}$ (as discussed in Section 2.1), where $I \neq 0$, three (potentially complex) roots of the function $g(s) + Is$ appear within the same interval. Within each interval, the roots of the function $g(s)+Is$ can be found by solving [24]:

$$(\eta_1)(1 + s\tau_2) + (\eta_2)(1 + s\tau_1) + Is(1 + s\tau_2)(1 + s\tau_1) = 0 \tag{47}$$

which can be expanded into the form of a 3rd order polynomial ($as^3 + bs^2 + cs + d = 0$) with coefficients

$$a = I\tau_1\tau_2$$

$$b = I(\tau_1 + \tau_2)$$

$$c = \tau_1\eta_2 + \tau_2\eta_1 + I$$

$$d = \eta_1 + \eta_2$$

whose roots (denoted s_k) can easily be found numerically. There are three roots (and hence $k = 1, 2, 3$) if the discriminant of this polynomial (i.e. $\Delta = 18abcd - 4b^3d + b^2c^2 - 4ac^3 - 27a^2d^2$) for the pair of modes (n and $n+1$) is positive (three real roots) or negative (one real and two complex conjugate roots). If the determinant evaluates to 0 the polynomial has a repeated root; a single repeated root if $3ac = b^2$ resulting in $k = 1$, otherwise there are two roots and $k = 1, 2$ [24]. Hence, the transient component $\gamma(t)$ can be expressed as

$$y_t(t) = \sum_{n=1}^{N_m - 1} \sum_k \frac{\sigma_0 \left(\omega\cos\phi + s_{n,k}\sin\phi\right)\exp(s_{n,k}t)}{s_{n,k}\left(I - \sum_m \frac{\eta_m\tau_m}{(1+s_{n,k}\tau_m)^2}\right)\left(s_{n,k}^2 + \omega^2\right)} \tag{48}$$

where $s_{n,k}$ refers to the kth root in the interval $1/\tau_n < s < 1/\tau_{n+1}$. The strain offset term is unaffected by inertia and can be expressed as:

$$\gamma_{off} = \frac{\sigma_0\cos(\phi)}{\omega\eta_0} \tag{49}$$

Generalising the above expressions for the strain response to a single-tone stress-controlled excitation to the response to an arbitrary stress-controlled waveform, following the same procedure as described in Section 2.1, we arrive at the following expressions for the strain response to a σOWCh waveform:

$$\gamma(t) = \gamma_{off}(t) + \gamma_p(t) + \gamma_t(t) \tag{50}$$

where,

$$\gamma_{off}(t) = \sum_i \sigma_i \left[\frac{H(t - t_i)\cos(\phi_i)}{\omega_i\eta_0} - \frac{H(t - t_{i+1})\cos(\phi_{i+1})}{\omega_i\eta_0}\right] \tag{51}$$

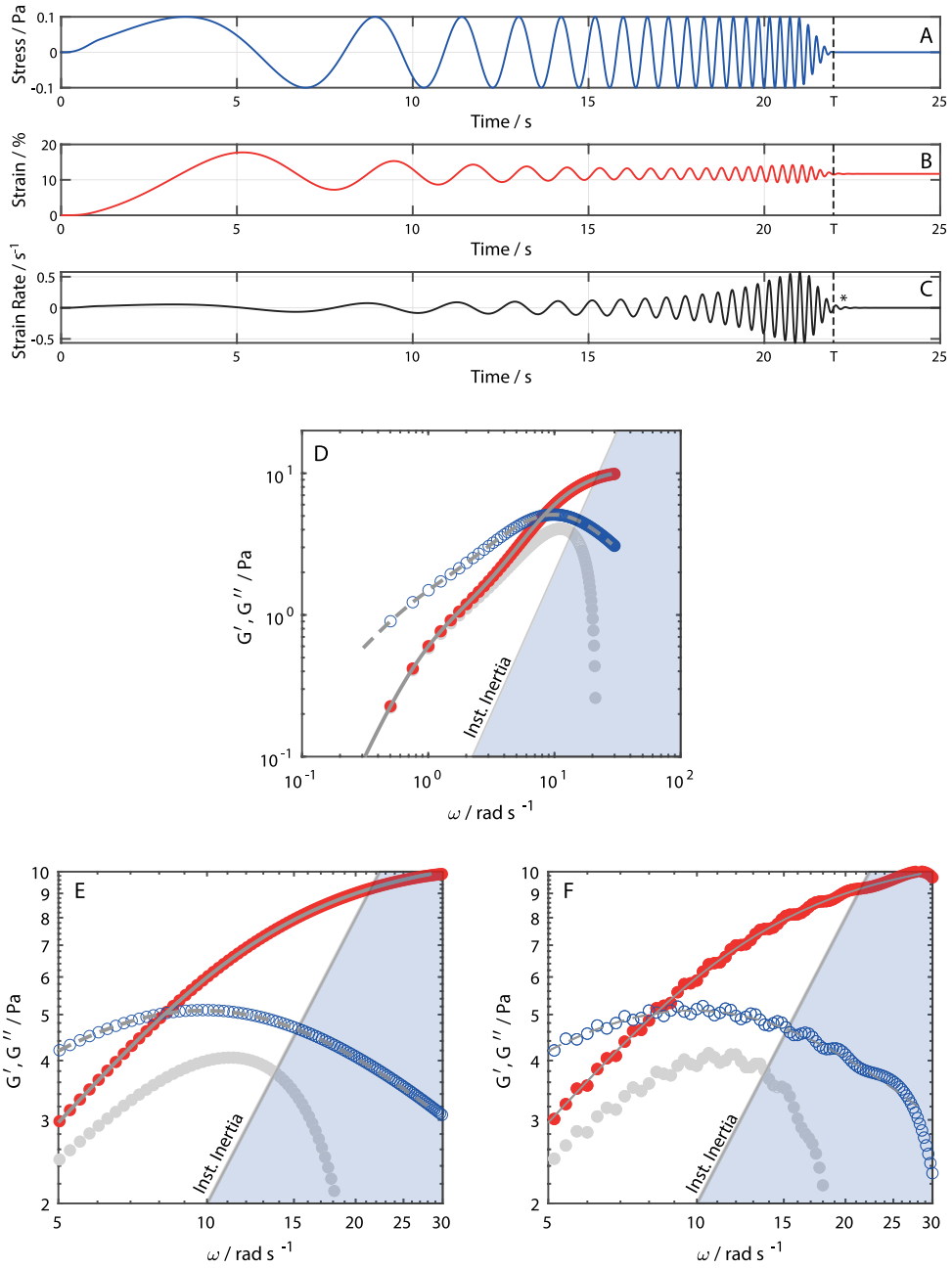

Fig. 3. Perturbation (A) and response (B&C) waveforms for a two mode Maxwell model (Eq. (33)) with $\tau_1 = 0.1$ s, $\tau_1 = 1$ s and $\eta_1 = \eta_2 = 1.0$ Pa s in the presence of an inertial term $I = 0.02$ Pa s^2. (D) Calculating $G^*(\omega)$ as using the σOWCh protocol, based on the FFT of the stress and strain-rate waveforms, generates raw loss (open blue) moduli that are in excellent agreement with their SAOS counterparts (dashed grey line) over the entire frequency range. Raw storage moduli (closed grey) agree with the SAOS data at low frequency but deviate significantly at high frequency due to the contribution from inertial term. Correction of the raw storage modulus by the addition of $I\omega^2$ returns the storage modulus to its expected behaviour (closed red). In (E), we show the high-frequency behaviour of the moduli when an additional period is added to the end of the waveform to allow the inertial effects to decay in contrast to (F) in which the strain waveform has been terminated at $T = 22$ s leading to truncation of the response waveform (marked $*$ in C). The shaded region in figures D-F shows regions in which inertial effects dominate the system response.

$$\gamma_t(t) = \sum_i \sum_{n=1}^{N_m-1} \sum_k \sigma_i \left\{ H(t-t_i) \frac{\left(\omega_i \cos\phi_i + s_{n,k} \sin\phi_i\right) \exp(s_{n,k}(t-t_i))}{s_{n,k}\left(I - \sum_m \frac{\eta_m \tau_m}{(1+s_{n,k}\tau_m)^2}\right)\left(s_{n,k}^2 + \omega_i^2\right)} - H(t-t_{i+1}) \frac{\left(\omega_i \cos\phi_{i+1} + s_{n,k} \sin\phi_{i+1}\right) \exp(s_{n,k}(t-t_{i+1}))}{s_{n,k}\left(I - \sum_m \frac{\eta_m \tau_m}{(1+s_{n,k}\tau_m)^2}\right)\left(s_{n,k}^2 + \omega_i^2\right)} \right\} \quad (52)$$

$$\gamma_p(t) = \sum_i \sigma_i \left\{ H(t-t_i) \times \left[\frac{(G_i' - I\omega^2)\sin(\phi_i + \omega_i(t-t_i)) - G_i'' \cos(\phi_i + \omega_i(t-t_i))}{(G_i' - I\omega^2)^2 + G_i''^2} \right] - H(t-t_{i+1}) \times \left[\frac{(G' - I\omega^2)\sin(\phi_{i+1} + \omega_i(t-t_{i+1})) - G_i'' \cos(\phi_{i+1} + \omega_i(t-t_{i+1}))}{(G_i' - I\omega^2)^2 + G_i''^2} \right] \right\} \quad (53)$$

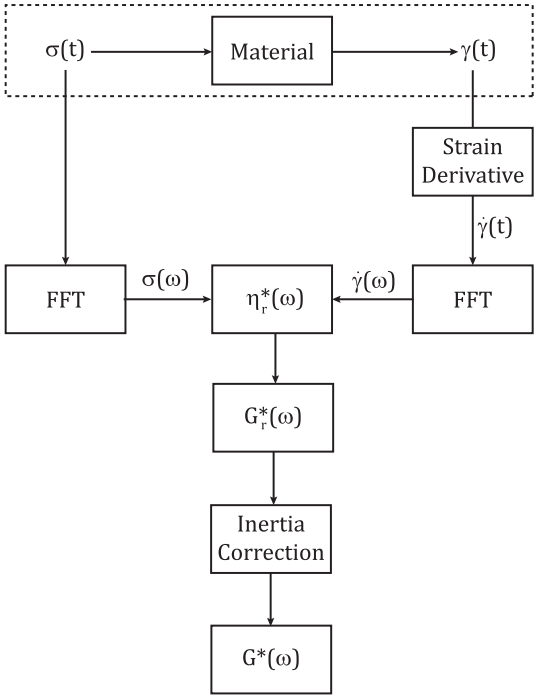

Fig. 4. Data processing algorithm for a stress-controlled σOWCh protocol.

Fig. 3 demonstrates the impact of system inertia on the strain (B), and strain rate (C) response to a stress-controlled chirp perturbation (A) for the same two-mode Maxwell model employed in Section 2.1.2 in the presence of instrument inertia (with $I = 0.02$ Pa s^2). There are three interesting features of this data that are not present in the inertialess case (Fig. 2). Firstly, a resonance effect causes the amplitude of the strain waveform to increase towards the end of the chirp. Secondly, the strain (and strain rate) signals persist beyond the chirp duration, T (shown as a dotted line), consequently a short post-chirp period (t_p) in which the stress is held at zero must be added to the perturbation waveform following the chirp to allow the strain-rate signal to return to zero (an additional, one-sided, window can be applied to the strain-rate signal over the interval $T < t < T + t_p$ during post-processing to force this transient response to zero if necessary). Applying Eq. (39) to the stress and strain-rate signals allows the calculation of a 'raw' complex modulus $G^*_{raw}(\omega)$, the real part of which contains an inertial contribution, $-I\omega^2$ (see Eq. (53)). The true storage modulus, $G'(\omega)$, can then be obtained from the real part of the $G^*_{raw}(\omega)$ as $G'_{raw}(\omega) + I\omega^2$ as per conventional SAOS experiments. A schematic of the proposed data processing algorithm for σOWCh is shown as Fig. 4.

When performing SAOS experiments using a CMT rheometer it is customary to consider either the 'raw phase angle' or the ratio of inertial to sample torques to identify data (typically that at high frequencies) in which the inertial contribution to torque dominates the total torque, thus preventing robust determination of $G^*(\omega)$. In an analogous manner, the raw phase angle can be calculated for data acquired from chirp experiments as $\text{atan}(G''/G'_{raw})$ where G'_{raw} denotes the real part of the apparent modulus G^*_{raw} as calculated via Eq. (39). TA Instruments documentation suggests that for an AR series rheometer, accurate inertia correction can be made where $\delta_{raw} < 155°$ [35] (confirmed for gelling materials by Hudson et al. [31]) whilst for the HR-30 rheometer, accurate inertia correction can be made for values of δ_{raw} as high as 175° [35]. Subfigures D and E show $G'(\omega)$ (red), $G''(\omega)$ (blue) and $G'_{raw}(\omega)$. It is clear that the recovered moduli are in excellent agreement with the analytical predictions. Fig. 3F shows the same data where the stress and strain waveforms have been truncated at T (i.e. no 'settling time' has been provided). Fresnel ripples are observed in both moduli because the periodicity of the underlying strain-rate data has been lost. It is interesting to note that in σOWCh a 'settling' period is required following the chirp whilst in a controlled-strain OWCh experiment (e.g. applied using an ARES-G2 rheometer) a delay is required at the start of the chirp waveform to allow settling of the torque transducer [7].

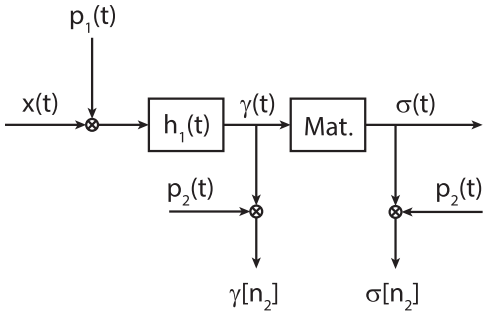

Fig. 5. Sampling and interpolation during data acquisition using an approximated chirp strain signal. $x(t)$ denotes the commanded chirp, $p_1(t)$ denotes the sampling function associated with the limited size of the LUT (with sampling rate 1024/T for a HR/DHR controlled stress rheometer). $h_1(t)$ denotes a first-order hold (i.e. linear interpolation) operation, Mat. denotes the 'material' transfer function and $\gamma(t)$ and $\sigma(t)$ denote the continuous 'approximate chirp' perturbation and response signals. $p_2(t)$ denotes the sampling function associated with data acquisition (488 pts/s herein) and $\gamma[n]$ and $\sigma[n]$ denote the discretely sampled strain and stress outputs as recorded by the instrument software.

2.3. Waveform construction

2.3.1. Digitisation

As discussed by Geri et al. [7], an important consideration when designing chirp waveforms is that the time-bandwidth product, $\text{TB} = T(\omega_2 - \omega_1)/2\pi$ is large in order to minimise the magnitude of ripples in the computed frequency spectra of the perturbation and response signals, and consequently, in $G^*(\omega)$. Since the frequency range of OWCh rheometry is limited by resolution and inertial considerations the TB requirement demands that long chirps be employed; a condition that cannot easily be satisfied when studying gelling systems as T is limited by the assumption that the rheological properties of the material do not vary throughout the duration of the chirp. However, a further limitation on the signal duration T exists as a consequence of the digitisation of the chirp waveform by the rheometer. For DHR/HR and MCR systems the command waveform is passed from the control software to the rheometer in the form of a look up table (LUT). The instrument firmware then interpolates between the LUT values in order to generate the continuous signal that is applied to the material as the perturbation waveform. The perturbation and response waveforms are then over sampled (often at a high rate) to generate the reported perturbation and response data that is processed to determine $G^*(\omega)$. The block diagram shown in Fig. 5 illustrates the sampling and interpolation processes that occur during waveform construction and data acquisition. There are two important sampling operations that must be considered.

The well-known Nyquist-Shannon criterion [37] defines the minimum sampling rate that must be used for data acquisition as twice the maximum frequency component of the signal. The HR/DHR and MCR systems sample torque and displacement at rates of (up to) 966 pts/s (HR/DHR) and (up to) 200 pts/s (MCR), far exceeding those required to satisfy the Nyquist-Shannon criteria at the highest chirp frequencies

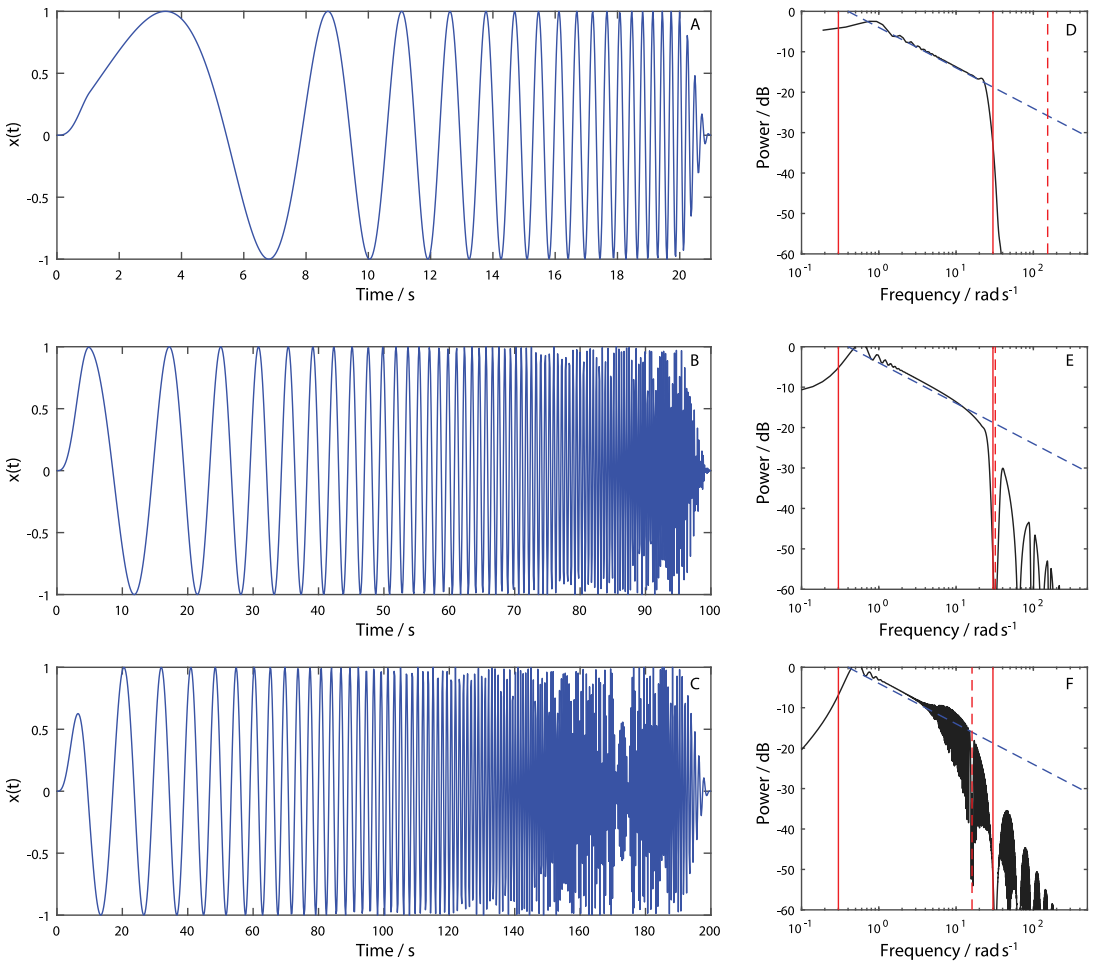

Fig. 6. Effect of increasing the signal duration T on perturbation waveform in time and frequency domains. In Figures A–C, we show perturbation signals generated using the algorithm presented as Fig. 5 with T = 21, 100 and 200 s respectively. In Figures D–E, we show the corresponding frequency domain representation obtained via a Fast Fourier Transform [36] (solid black lines). In figures D–E, solid red lines show the frequency band of the command waveform, the dashed red line shows the Nyquist frequency associated with waveform generation (i.e. based on the sampling rate for p_1) and the dashed blue line shows the scaling of a 'pink' power spectrum for reference. For chirps A–C, $N = 1024$, hence chirps B and C do not satisfy the oversampling criterion, with $R = 1.07$ and $R = 0.54$, respectively.

that may be applied using conventional rheometers. However, the generation of the LUT also involves a sampling operation (shown as p_1 in Fig. 5).

The LUT that is generated by the rheometer software has N entries which are uniformly distributed over the chirp duration $(T + t_p)$, hence the sampling rate for waveform generation is $p_1 = N/(T + t_p)$. The value of N is instrument-specific and, whilst for the ARES-G2 rheometer $N > 32{,}000$, for the DHR/HR series of instruments $N = 1024$ and for the Anton Paar MCR series (in both CMT and SMT configurations), $N \approx 2048$. In the frequency domain, this sampling operation generates aliases of the spectrum of the desired signal that are centred at integer multiples of the sampling frequency $(1/p_1)$. However, the subsequent interpolation of the LUT (convolution of the sampled time domain signal with a triangular pulse) has the effect of multiplying the frequency domain spectrum with a $sinc^2(\omega)$ function [38] which has *zeros* at integer multiples of the sampling frequency $(1/p_1)$. Consequently, inappropriate selection of p_1 (because of an excessive chirp duration, T for the given LUT size, N) causes (i) power to be lost to higher 'aliased' frequencies outside of the chirp bandwidth and (ii) the loss of all power at frequencies around $1/p_1$. In the time domain, the approximate chirp waveform loses its smoothness and may, at high frequencies, completely skip entire oscillations causing rapid accelerations and preventing appropriate inertial correction. Fig. 6 shows perturbation waveforms generated using LUTs with $N = 1024$ for $T = 21, 100, 200$ s as figures A–C. Whilst the 21 s chirp is accurately approximated by the algorithm, the longer chirps show significant deviations from the expected waveform. Fig. 6D–E shows the corresponding power spectra with D showing the characteristic 'pink' power spectrum of a chirp (shown as a dashed blue line decaying inversely with frequency) for the accurately reconstructed chirp signal and E/D showing significant deviations from the expected power spectrum.

An operational limit for the chirp time, T, based on ω_2 can hence be determined by considering an oversampling criterion based on the Nyquist frequency of the waveform (i.e. $2 \times \omega_2/2\pi = \omega_2/\pi$) and the sampling rate associated with LUT generation $(N/(T + t_p))$, i.e. we evaluate the ratio, $R = \pi N/\omega_2(T + t_p)$. A value of $R > 4$ is found to generate adequate approximations to the desired chirp signal (see Supplementary Materials). Furthermore, since ω_1 and T are effectively linked by a relationship of the form $T = 2\pi/\omega_1$, there is a single degree of freedom when designing chirp waveforms where the objective is to probe as wide a frequency range as possible (a limitation not encountered for the ARES-G2 for which N is not limiting). For example, one may specify ω_1 to be 0.1 rad/s, thus T should be at least $T = 2\pi/0.1 = 62.8$ s, and, for $t_c = 1$ s and $R = 4$, ω_2 is limited to $\omega_2 \approx 12$ rad/s for the TA Instruments DHR/HR series ($N = 1024$). Fig. 7

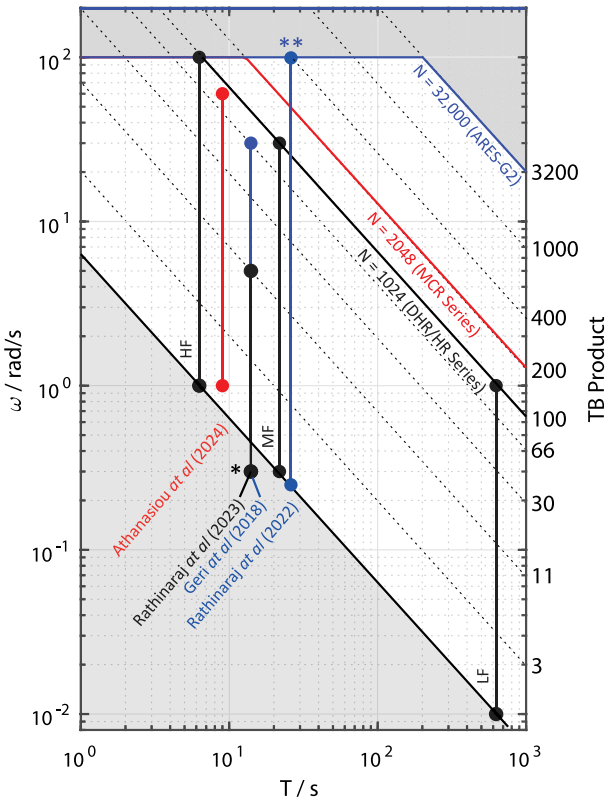

Fig. 7. Time-bandwidth design space of OWCh waveforms. The lower bound is set by $2\pi/T$ whilst the upper bound is set by $R = 5$ and depends on the size of the look-up table (N) employed by the rheometer being used. Diagonal contours denote lines of constant time-bandwidth product, TB, (with $\omega_1 = 2\pi/T$). A maximum ω_2 of 100 rad/s has been utilised in generating this figure. Operational limits (associated with resolution and inertia) will also bound the available design space, however, since these depend on the material being studied we do not attempt to include them in this figure. The chirp waveforms employed in the present study are show as LF, MF and HF (low, medium and high frequency) whilst those employed by Geri et al. (2018) and Rathinaraj et al. (2022) using an ARES-G2 [7,19], Rathinaraj et al. (2023) using a DHR-30 [20] and Athanasiou et al. using an MCR702 [15] are shown for reference. [Note: *Whilst the studies of Geri et al. (2018) and Rathinaraj et al. (2023) used chirps with $\omega_1 = 0.3$, only data for $\omega > 0.45$ rad/s was reported since $\omega_1 < 2\pi/T$ which is consistent with the operating window reported in the figure, **The study of Rathinaraj et al. (2023) [19], extending the use of chirp waveforms to orthogonal superposition experiments, employed external hardware for which the size of the LUT was not reported].

shows the presently accessible chirp parameter space for rheometers with different sizes of lookup table (LUT) evaluated using $R = 5$. The lower boundary is determined by the relationship $\omega = 2\pi/T$, whilst the upper boundary depends on the available LUT size (as shown by the value of N displayed). Vertical lines represent chirp signals that have been applied in the literature to date, in terms of their duration (T) and frequency band ($\omega_2 - \omega_1$). Diagonal lines thus represent a constant Time-Bandwidth product, $TB = T(\omega_2 - \omega_1)/2\pi$ (with values shown on the right-hand ordinate axis), where ω_1 is determined as $2\pi/T$ (i.e. the minimum frequency for a given chirp duration). Geri et al. [7] demonstrated that maximising TB is an important aspect of chirp waveform design. It is evident from the figure that as the signal duration is decreased (i.e. moving to the left in the design space shown) the time-bandwidth values and the frequency band accessible become increasingly constrained.

In their work implementing OWCh using an MCR702 operating in SMT mode, Athanasiou et al. [15] addressed the limited size of the LUT by limiting their chirp duration to 10 s for a chirp with $\omega_2 = 60$ rad/s.

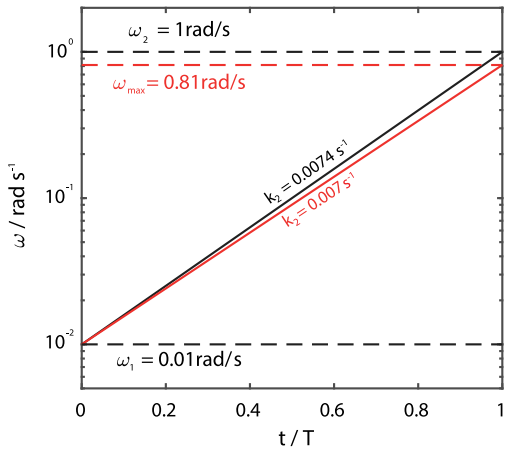

Fig. 8. Effect of truncation of logarithmic skew rate (k_2) for low-frequency chirps. Including insufficient significant numerical precision for k_2 into the waveform definition results in a slightly slower than anticipated evolution of the instantaneous frequency $\omega(t)$. This effect is compounded by the desired exponential variation in frequency, the waveform imposed by the instrument does not probe frequencies above ω_{max} thus generating noisy data in the frequency range $\omega_{max} \leq \omega \leq \omega_2$.

Such a chirp (with $N = 2000$)[1] has an oversampling ratio of around 12 thus satisfying the proposed criterion.

2.3.2. A note on the importance of defining the Logarithmic Skew Rate to sufficient numerical precision

An important parameter in defining the chirp waveform is the Logarithmic Skew Rate, k_2, originally defined in Eq. (1) and given by:

$$k_2 = \frac{1}{T} \ln\left(\frac{\omega_2}{\omega_1}\right) \tag{54}$$

which determines how quickly the angular frequency evolves on a logarithmic scale during the chirp. When using low-frequency chirps, one must ensure that this parameter appears within the expressions that define the chirp to a sufficient number of significant digits. For example, a chirp with a specified frequency range 0.01 rad/s $\leq \omega \leq$ 1.0 rad/s and $T = 628.3$ s should have $k_2 = 0.0074$ s^{-1}. Truncating this to $k_2 = 0.007$ s^{-1} due to, for example, the limited number of characters that may be used to specify the input signal on the TA Instruments ARES-G2 rheometer, generates a waveform for which $\omega_2 = 0.81$ rad/s (see Fig. 8). Hence, no power is present in the perturbation waveform above 0.81 rad/s resulting in significant noise appearing in the moduli at this point. The DHR/HR series of rheometers are less restrictive in terms of the number of characters available for waveform definition and hence k_2 may be input at a precision greater than three decimal places.

Having now defined an appropriate data processing algorithm, inertial correction procedures, and guidelines for chirp design we now proceed to demonstrate the use of σOWCh in a range of materials using the TA Instruments DHR/HR series rheometers.

3. Experimental

3.1. Rheometry

Two rheometers, a TA Instruments HR-30 rheometer (at Swansea) and a TA Instruments DHR-3 (at MIT) were employed for all experiments reported herein. Geometry selection was sample specific and

[1] Whilst the MCR has a LUT size of $N = 2048$ this can be reduced by the operator.

Table 1
Chirp parameters for the three σOWCh chirps employed herein.

Chirp	ω_1 [rad/s]	ω_2 [rad/s]	T [s]	R
Low Frequency (LF)	0.01	1.0	628.0	5.1
Mid Frequency (MF)	0.30	30.0	21.8	4.9
High Frequency (HF)	1.0	100	6.28	5.1

is noted in Sections 3.2 to 3.7. Low viscosity silicone oil was used to prevent evaporation of aqueous samples. Samples were loaded to the temperature-controlled (Peltier) lower plate of the rheometer before the upper geometry was lowered into place. Experiments were performed at a stress amplitude within the LVR as determined via amplitude sweeps at frequencies of 0.1 rad s^{-1} and 1 rad s^{-1} (data not shown) unless otherwise stated below. The additional requirement of satisfying the oversampling criteria (see Section 2.3) prevented the use of a single chirp covering four decades of frequency (0.01 rad/s $\leq \omega \leq$ 100 rad/s), however, three sequential chirps as detailed in Table 1 and designated as LF, MF and HF (i.e. low-frequency, mid-frequency and high-frequency chirps, respectively) on Fig. 7 were employed. The three chirps were applied over a total duration of approximately 11 min, a conventional frequency sweep approach (with five points per decade, three cycle sampling, and one cycle of conditioning time) requires approximately two hours to acquire data over the same frequency range and achieves a far lower data density. Conventional frequency sweep (FS) data was acquired as a basis for confirming the accuracy of the σOWCh protocols. In all experiments, chirp rheometry and conventional FS rheometry were performed on the same sample to minimise the impact of loading errors when comparing the results of the two techniques. For some samples, terminal Maxwell-like viscoelastic behaviour was evident below $\omega \approx 0.1$ rad/s and hence the range of the FS was truncated to 0.1 rad/s $\leq \omega \leq$ 100 rad/s.

3.2. Silicone oil

3.2.1. Sample & geometry

The first, and simplest, material response that we consider is that of the Newtonian fluid. A 970 mPa s Silicone Oil (Brookfield) was tested at 25 °C using a TA Instruments HR-30 fitted with a 60 mm 2° aluminium cone with a truncation gap of 52 μm.

3.2.2. Results & discussion

Fig. 9 shows conventional FS data (lines) and the results of the LF, MF and HF σOWCh experiments. It is clear that the G'' data are in excellent agreement across the entire frequency range with $\delta \geq 89.2°$ being observed for all data. Whilst non-zero values of G' are present for both the conventional and OWCh-based experiments, these data lie close to the operational limits of the rheometer. The operational limit associated with instrument inertia has been determined following Ewoldt et al. [25] using $G'_{min}(\omega) = \varepsilon I \omega^2$ where $\varepsilon = 0.1$. For this value of ε, only 10 % of the total torque applied to the system is used to deform the sample. Beyond this point, inertia correction (as per Section 2.2) is unreliable due to uncertainty in precisely determining the value of I [25,31]. At $\omega < 10$ rad/s, both OWCh and FS data appear to show G' above the inertial limit. Whilst for strain controlled experiments, a minimum value of G (either G' or G'') can be determined based on torque resolution [25], for stress controlled protocols, the minimum value of G is associated with the maximum strain amplitude that may be applied to the material (defined by the extent of the linear viscoelastic region). For silicone oils, the extent of the linear range is large and hence the apparent non-zero values of $G'(\omega)$ are likely due to a deviation from true viscometric conditions (e.g. the presence of a small asymmetry in the sample free surface [25]). Importantly, the artifact in the chirp-based determination of $G'(\omega)$ is acceptably small, being of a similar magnitude to that in the conventional FS data.

3.3. Polydimethylsiloxane

3.3.1. Sample & geometry

As an example of a (room temperature) melt system, a polydimethylsiloxane (PDMS) sample was studied using a HR-30 fitted with a 20 mm 2° stainless steel cone with a truncation gap of 48 μm

3.3.2. Results & discussion

Fig. 10 shows excellent agreement between the dynamic moduli of the PDMS sample as measured using FS and σOWCh-based procedures over the entire frequency range studied. The operational limit associated with instrument inertia is also shown and was determined as described in Section 3.2.2.

3.4. Polyethylene oxide solution

3.4.1. Sample & geometry

As an example of a concentrated polymer solution ($c > c^{**}$, where c^{**} denotes the second critical concentration [39]), a 2.5 wt% aqueous solution of poly(ethylene oxide), PEO, (4×10^6 g/mol, Sigma Aldrich, 189 464) was studied. Appropriate amounts of PEO powder and type I deionised water were combined to form the desired concentration using a magnetic stirrer at room temperature for ≈ 24 h [39]. Any bubbles incorporated into the PEO during preparation were removed by degassing the sample in a vacuum chamber. Samples were stored at room temperature before being loaded directly onto the temperature-controlled (20 °C) Peltier plate of a TA instruments HR-30 rheometer fitted with a 60 mm 2° aluminium cone with truncation 52 μm.

3.4.2. Results & discussion

Fig. 11 compares the results of the consecutive LF, MF and HF chirps with equivalent data acquired using a conventional FS experiment. As observed for the silicone oil and PDMS experiments, excellent agreement is observed across the entire frequency range.

3.5. Worm like micelles

3.5.1. Sample & geometry

A 4.1 wt% cetylpyridinium chloride in sodium salicylate sample was prepared and studied as an example of a worm-like micellar (WLM) system. Cetylpyridinium chloride (CPyCl) and sodium salicylate (NaSal) (both from Sigma-Aldrich) were dissolved at a molar ratio of 2:1 in 0.5 M sodium chloride (NaCl) (Sigma-Aldrich) solutions prepared using deionised water. The samples were stirred for 24 h at 40 °C (in a sealed beaker atop a heated plate) to completely disperse the powder. All chemicals were used as received without further purification. This WLM formulation has been reported to display viscoelastic shear thinning characteristics in contrast to those at higher CPyCl/NaSal concentrations which have been shown to exhibit shear banding characteristics [40–42]. In the present work we restrict our attention to 'non-shear banding' formulations. Samples were stored at room temperature before being loaded directly onto the temperature-controlled lower plate of a TA instruments HR-30 rheometer fitted with a 60 mm 2° aluminium cone with truncation 52 μm. This system served the additional purpose of providing an experimental verification of the modelling efforts of Section 2.2, since its linear viscoelastic behaviour can be adequately captured by a two-mode Maxwell model - thus allowing the expressions derived in Section 2.2 to be used to predict the system response to a σOWCh waveform that can subsequently be compared with the experimental response following Ogunkeye et al. [24].

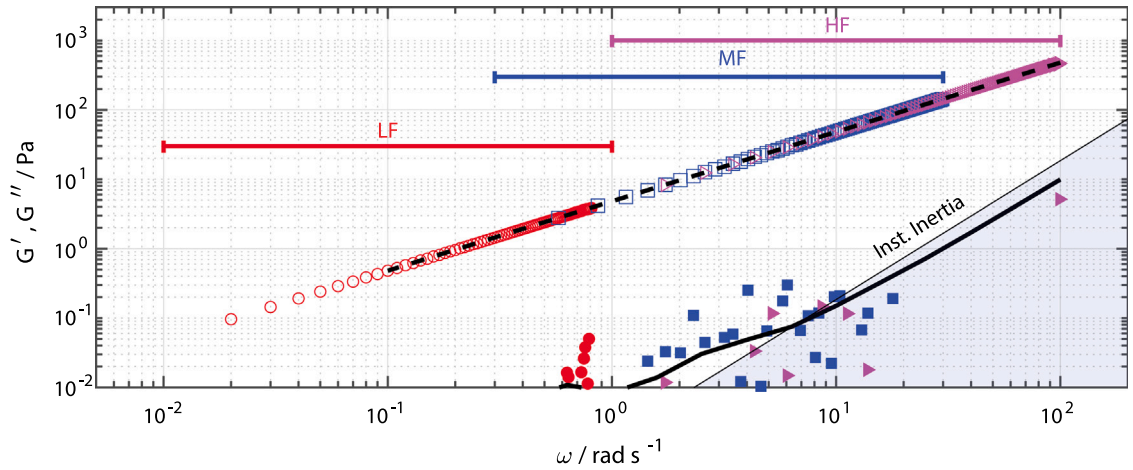

Fig. 9. Comparison of FS and stress-chirp (σOWCH) based data acquired using a HR-30 rheomter for a 0.987 Pa s Silicone Oil. Storage and loss moduli (G' and G'') are shown as filled and open symbols respectively. The instrument inertia limit line has been determined as $G'_{min}(\omega) = \varepsilon I \omega^2$ where $\varepsilon = 0.1$, following [25].

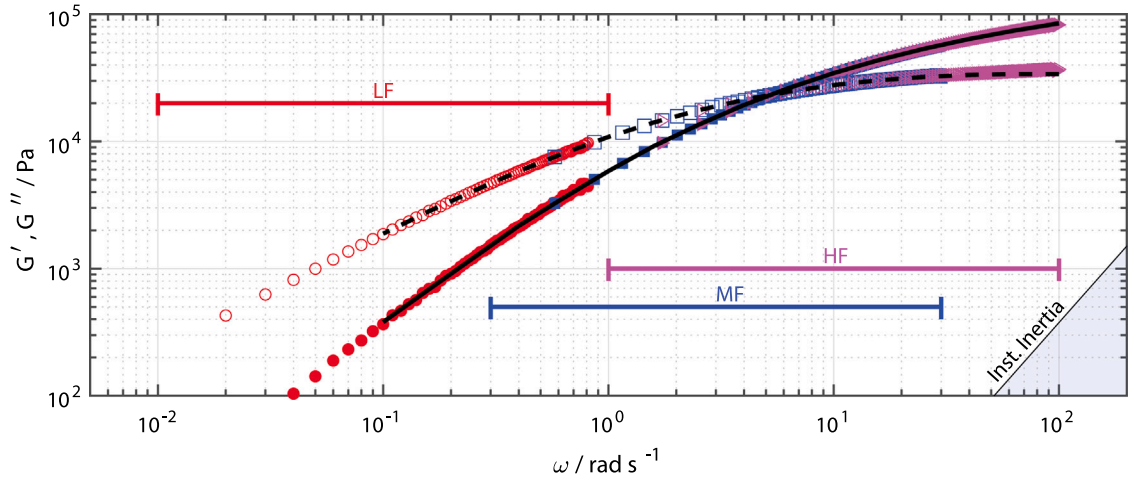

Fig. 10. Comparison of FS and stress-chirp (σOWCH) based data acquired using a HR-30 rheometer for a PDMS sample. Storage and loss moduli (G' and G'') are shown as filled and open symbols respectively. The instrument inertia limit line has been determined as $G'_{min}(\omega) = \varepsilon I \omega^2$ where $\varepsilon = 0.1$, following [25].

3.5.2. Results & discussion

Fig. 12 demonstrates excellent agreement between the stress chirp and FS-based dynamic moduli. There is some discrepancy between the moduli at high frequency, however, as can be seen from Fig. 12, the discrepancy appears close to the operational limit associated with instrument inertia.

In order to verify the modelling efforts of Section 2.2, the FS data was fitted to a two-mode Maxwell model (with $\tau_1 = 0.17$ s, $\tau_2 = 0.017$ s, $\eta_1 = 5.85$ Pa s and $\eta_2 = 0.135$ Pa s) as shown in Fig. 13 (this figure also shows moduli associated with the longest mode in isolation as dashed lines, demonstrating the need for both modes to fit the data adequately). The two-mode Maxwell model was then used to *predict* the response of the material to a stress-controlled chirp signal (HF chirp) using Eqs. (50) to (53) with $I = 0.0185$ Pa s^2, i.e. the calibrated inertia constant of the instrument. The predicted response to the HF chirp signal is shown in red on Fig. 14. The corresponding chirp experiment was then performed and the results are also shown, in grey, on Fig. 14. No fitting of the experimental data (after initial parameterisation of the model based on the SAOS data of Fig. 13) was undertaken. The predicted response to the stress-controlled chirp is in excellent agreement with the measured response. It is especially noteworthy that resonant effects (seen at $t > 4.5$ s) are very well captured by the model providing confidence in the derivation of Section 2.2.

3.6. Gelatin

3.6.1. Sample & geometry

Samples of 10 wt% gelatin were prepared by combining appropriate quantities of gelatin powder (Fisher G/0150/53) and type I deionised water preheated to 60 °C. Each sample was agitated for two minutes before being placed into a 60 °C water bath for 45 min (with further agitation at 10 min intervals) to ensure complete dissolution of the gelatin powder. Aliquots were kept at 60 °C for no longer than 45 min at a time to prevent degradation of the gelatin solutions. The gelatin samples were stored at 4 °C in a refrigerator until required. To prepare for testing, samples were removed from the refrigerator and placed

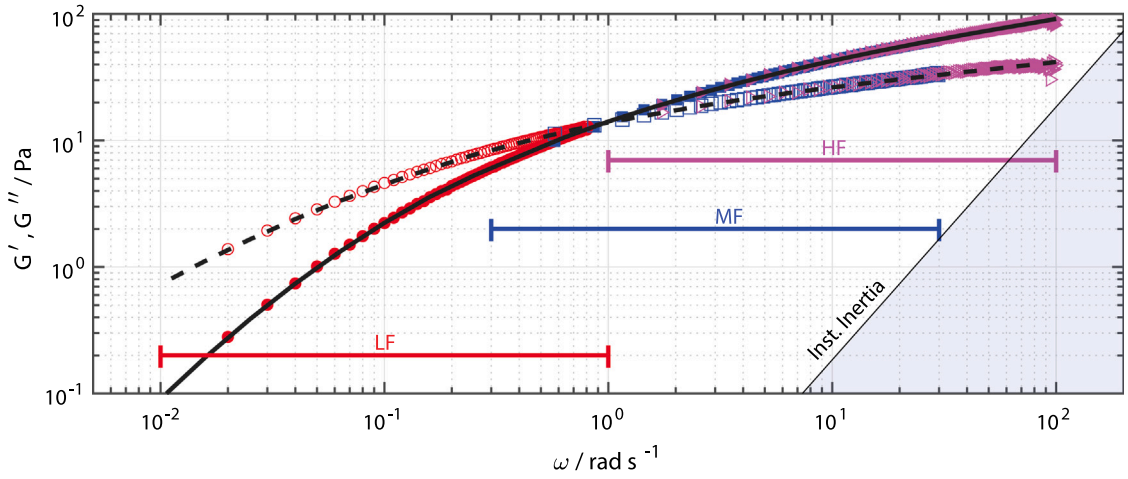

Fig. 11. Comparison of FS and stress- chirp (σOWCH) based data acquired using a HR-30 rheometer for a 2.5 wt% PEO sample. Storage and loss moduli (G' and G'') are shown as filled and open symbols respectively. The instrument inertia limit line has been determined as $G'_{min}(\omega) = \varepsilon I \omega^2$ where $\varepsilon = 0.1$, following [25].

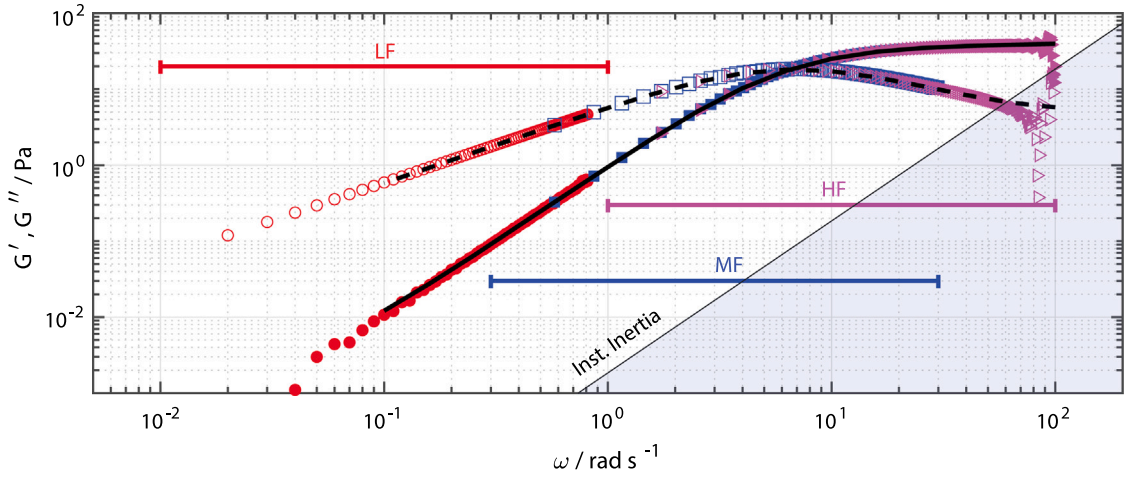

Fig. 12. Comparison of FS and σChirp based data acquired using a HR-30 rheomter for a WLM sample. Storage and loss moduli (G' and G'') are shown as filled and open symbols respectively. The instrument inertia limit line has been determined as $G'_{min}(\omega) = \varepsilon I \omega^2$ where $\varepsilon = 0.1$, following [25].

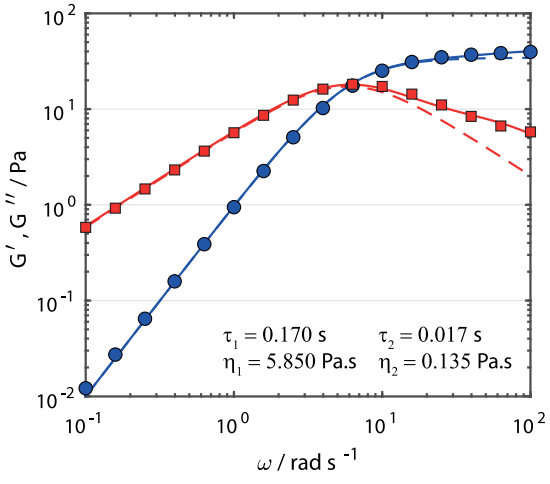

Fig. 13. Conventional frequency sweep based dynamic moduli for a WLM system with a two mode Maxwell fit (solid lines). Dashed lines show the linear viscoelastic moduli calculated from the longest mode only, demonstrating that two modes are necessary to fit the data.

into a 60 °C water bath for 45 min. A 60 mm aluminium plate with a gap of 300 μm (sufficiently small to ensure the 'gap loading' criterion was met) fitted to a HR-30 rheometer was used with the medium frequency range (MF) chirp signals (as detailed in Table 1) with stress amplitude $\sigma_0 = 0.1$ Pa being applied to the material every 40 s (a delay of 25 s associated with data transfer and storage in the rheometer operating software package TRIOS 5.7.2.101 prevents more rapid data acquisition).

3.6.2. Results & discussion

Fig. 15A shows the results of the repeated chirps in terms of the evolving phase angle as a function of time. This representation of the data allows the gel point, which marks the establishment of a sample-spanning network, to be easily determined as the time point at which the phase angle is independent of frequency. At this point, a critical gel exists for which G' and G'' both scale with the same power law in frequency $G' \sim G'' \sim \omega^{\alpha}$. The value of the power law exponent, α, can be related to the microstructure of the incipient gel network [18]. Note that data at 10 logarithmically spaced frequencies is shown on Fig. 15A for visual clarity, despite data at over 80 discrete frequencies being available from the σOWCh experiment. Fig. 15B shows the measured

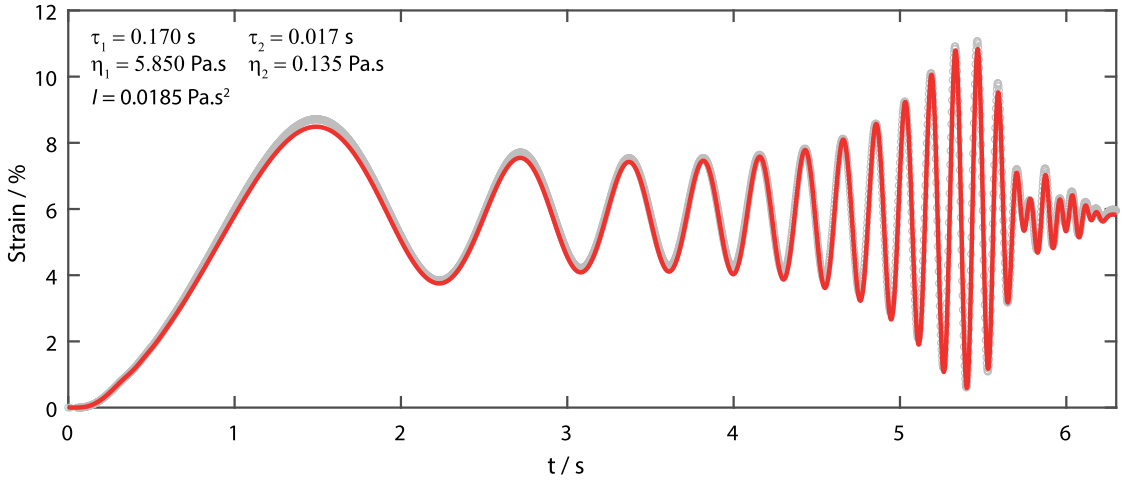

Fig. 14. Prediction (red line) of the response of WLM (modelled as a two mode Maxwell material as shown in Fig. 13) to a stress controlled chirp perturbation with $\omega_1 = 1$ rad/s, $\omega_2 = 100$ rad/s, $T = 6.3$ s and $\sigma_0 = 10$ Pa using a controlled stress single head instrument with inertial constant $I = 0.0185$ Pa s^2. Grey symbols show experimental data for the same system demonstrating excellent agreement with the prediction and establishing confidence in the modelling approach of Section 2.2. It is important to note that no calibration of the model was performed based on the experimental chirp data and the red line may be considered to be a prediction.

values of the LVE moduli at the GP (t = 11.9 min) with identical power-law scaling (with $\alpha = 0.71$) being clearly evident (all available frequencies are shown).

As discussed in Section 1, the rheological characterisation of transient systems, using conventional FS or Chirp-based rheometry, requires that the period of the perturbation waveform be short relative to the timescale over which the material properties are changing. Winter et al. [43] proposed a dimensionless Mutation number characterising the time rate of change of material properties (on a dimensionless, logarithmic scale), $d \ln G/dt$, with the duration of the applied waveform ΔT, where G can be any material property, usually $G'(t)$ or $G^*(t)$,

$$N_{mu} = \frac{\Delta T}{G}\frac{dG}{dt} \tag{55}$$

with $N_{mu} < 0.15$ often being considered an appropriate criteria for confirming the validity of the LTI assumption [44]. For the data presented in Fig. 15, the Mutation number at the gel point ranges from $N_{mu} = 0.141$ at the lowest frequency to $N_{mu} = 0.056$ at the highest frequency. A closely related, though distinct, issue concerns data interpolation. Whilst the Mutation number ensures that individual data points are valid, identification of the gel point typically requires some degree of data interpolation in either $G^*(\omega, t)$ or $\delta(\omega, t)$. Hawkins et al. [4] addressed this problem by defining an 'interpolation criterion' which compares the experiment time, t_{exp} (i.e the time required to generate one complete FS, including any conditioning or data transfer delays) to the material gel time, t_g, as

$$N_{int} = \frac{t_{exp}}{t_g} < 0.1 \tag{56}$$

Whilst this criterion is unlikely to be universal (since it does not consider the local rate of change of material properties around the GP) it has been shown to be valid for gelatin systems [4]. For the data shown in Fig. 15, $N_{int} \approx 0.056$. Artefacts associated with sample mutation and interpolation should be carefully considered, alongside the oversampling criterion, when determining the chirp duration and frequency content for a particular experiment.

3.7. Laponite (colloidal gel)

3.7.1. Sample & geometry

An aqueous suspension of 3.5 wt% hectorite clay (LAPONITE® RD) was prepared using dry Laponite powder and a 5 mM Sodium Chloride (NaCl) solution. The corresponding amount of Laponite powder was added gradually in small portions to the ionic aqueous solution and mixed using a high shear mixer (Ultra-Turrax T 50 basic mixer, IKA) at 10,000 rpm, the pH of the suspension was measured to be approximately 8.5. The suspension was then transferred to a rolling mill and left for one day to ensure homogeneity and allow any entrained air to separate. Subsequently, the suspension was stored in a Borosilicate glass bottle for 2 years. Rheometric measurements were performed using a TA Instruments DHR-3 Rheometer, with a temperature-controlled bottom Peltier plate, and an upper 60 mm diameter, 2° aluminium cone with truncation gap 58 μm. After loading the sample to the rheometer, the cone-and-plate fixture was enclosed within a solvent trap to prevent solvent evaporation from the sample. Before the experiment, the Laponite suspension was presheared by using a shear rate of 500 s^{-1} for 30 s. This preshearing stage was essential for achieving reproducible data and to 'letherize' the material and reset the internal 'material clock'. The test protocols and data acquisition were performed using the rheometer software (TRIOS v5.7.0.1).

3.7.2. Results & discussion

Fig. 16 illustrates the evolution of the storage and loss moduli of the Laponite sample at a temperature of T = 25 °C, as determined through a series of eight consecutive stress chirps imposed. Each chirp was designed considering the mid-frequency (MF) range i.e., $\omega_1 = 0.3$ rad/s to $\omega_2 = 30$ rad/s, with a duration of 14 s, resulting in a time-bandwidth product, TB $\approx$ 66. The input stress amplitude was set at $\sigma_0 = 10$ Pa, which is within the linear viscoelastic regime ($\sigma_0 \leq 40$ Pa), as confirmed by an oscillatory stress- amplitude sweep experiment at a frequency 6 rad/s. A Tukey window with tapering parameter, $r = 10\%$ was used, and each chirp was followed by a 2-s post-chirp period to provide sufficient time for residual transient effects to decay, i.e., to allow sufficient time for the strain rate to decay to zero and the strain to return to a constant offset value. Notably, the wait time — also known as the aging time of the material sample — differs for each chirp test (which increased steadily from chirp to chirp), following

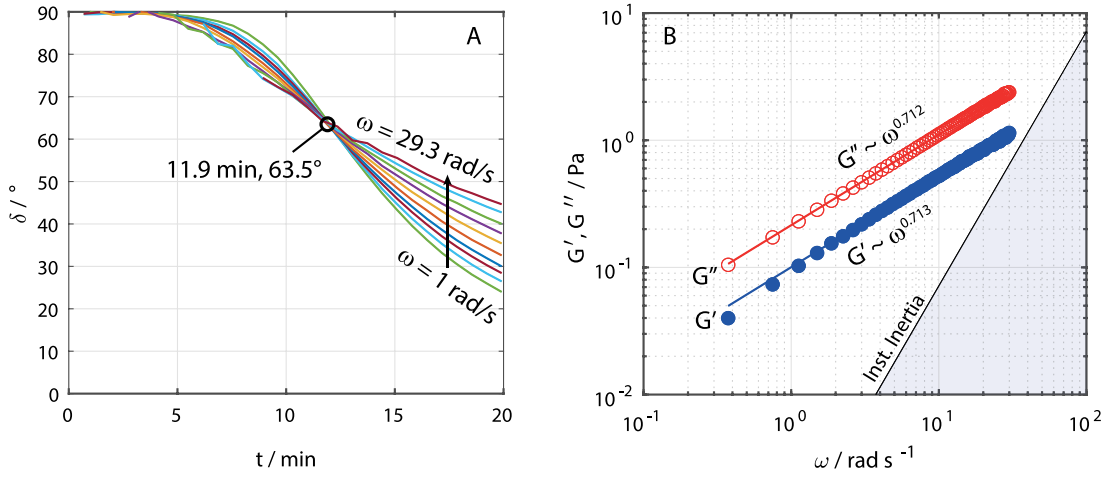

Fig. 15. (A) Transient gelation data expressed as the evolving phase angle ($\delta(\omega, t)$) as a function of time at 10 logarithmically spaced frequencies (1.0 rad/s $\leq \omega \leq$ 29.1 rad/s) with the Gel Point (GP) identified at the frequency independent point. (B) Dynamic moduli as a function of frequency, measured using a stress chirp with $\omega_1 = 0.4$ rad/s, $\omega_2 = 30$ rad/s, $T = 15.708$, $t_p = 1.0$ s and $\sigma_0 = 0.1$ Pa (such that $TB = 74$ and $R = 6.4$), at the GP demonstrating identical power law scaling with $G' \sim G'' \sim \omega^{0.71}$. The instrument inertia line (shown in subfigure B) has been determined as $G'_{min}(\omega) = \varepsilon I \omega^2$ where $\varepsilon = 0.1$, following [25].

the preshearing process. As depicted in Fig. 16, the storage modulus, $G'(\omega, t_w)$ increases as the material ages, indicated by a transition in colouring from light orange to black-filled circles. A weak power-law dependence on frequency is also observed. On the other hand, the loss modulus, $G''(\omega, t_w)$ demonstrates the opposite trend as the waiting time (or material age) increases. At lower frequencies, the loss modulus shows a decreasing trend or a negative slope, reaching a local minimum at a frequency of $\omega = 10$ rad/s. Beyond this point, the loss modulus begins to increase with increasing frequencies. Similar trends were also observed by Rathinaraj et al. [20] in a recent study on bentonite dispersions. They attributed this upturn in the loss modulus at higher frequencies to instantaneous, non-aging background effects, such as those arising from the solvent or other non-aging viscous contributions to the material response. These observed trends in the evolution of the storage and loss moduli are consistent with previous findings on dispersions reported by Pilavtape et al. [45] and Shukla et al. [46].

4. Summary

4.1. Stress controlled chirp rheometry

The use of chirp-based rheometry is gaining popularity. However, to date, all reported implementations have employed either separate motor transducer (SMT) instruments [7,15,19] or single-head instruments in stress-controlled operating mode for a specific class of materials (i.e. yield stress type materials [20]). In the latter study, the specific linear elastic response of the yield stress material below yield enabled the existing OWCh algorithm [7] to be employed, but its general application to stress-controlled signals results in poor quality data. In the present work, we have undertaken a detailed mathematical analysis of stress-based frequency-modulated rheometry (σOWCh) using single-head/combined motor transducer rheometers and have developed novel data processing algorithms and operational guidelines for waveform design. These protocols permit chirp-based rheometry to be rapidly applied to a much wider range of materials without reliance on displacement feedback loops (which are typically machine-specific and optimised for viscometric and conventional SAOS experiments) thus overcoming a significant barrier to the widespread adoption of OWCh. There are three important aspects that must be considered when performing stress-controlled chirp experiments which we summarise below.

- The strain response to the start-up of stress-controlled oscillations includes the presence of a strain offset (which depends on the amplitude and frequency of the applied waveform as well as the zero shear viscosity of the sample) about which the strain oscillates [22–24]. Typically, the offset is removed as part of the conventional data processing undertaken by rheometer software. However, this is not generally feasible for chirp-based waveforms and, as such, the strain response to a stress chirp contains a time varying offset term which can render the results of a standard OWCh analysis (based on discrete frequency transforms of the measured stress and strain waveforms) incoherent. However, as we have shown in Section 2.1, this limitation can be easily remedied by evaluating the complex viscosity using the instantaneous time rate of change of the strain $\dot{\gamma}(t)$ rather than the complex modulus (which may be subsequently calculated using the relation $G^* = i\omega\eta^*$).
- Chirp waveforms are passed from the rheometer software to the instrument in the form of a look up table (LUT). Whilst the ARES-G2 rheometer has a LUT with approximately 32,000 points, the TA Instruments DHR/HR series rheometers and Anton Paar MCR Series rheometers have far smaller LUT sizes, limited to 1024 and 2048 points, respectively. Hence, chirp waveform design must be carefully undertaken in order to ensure that the commanded signal sufficiently approximates the desired chirp waveform. In Section 2.3 it has been demonstrated that an oversampling ratio $R = \pi N/\omega_2(T + t_c) > 4$ is sufficient for performing chirp experiments.
- The use of single-head rheometers requires that instrument inertia effects also be considered. Sections 2.2 and 3 demonstrate that the operational limits associated with instrument inertia for chirp waveforms are similar to those for conventional frequency sweep experiments and can be corrected in the same fashion (by adding the term $I\omega^2$ to the raw value of G'). Importantly, a further complication arises as a consequence of inertia which causes the strain waveform to persist beyond the duration of the applied stress chirp (due to the transient response of the inertio-elastic system) which necessitates data to be acquired for a short period (~1 s) beyond the chirp duration, T.

The waveform design and analysis protocols described herein have been implemented in a Matlab Graphical User Interface, SUMIT OWCh (i.e. Swansea University/Massachusetts Institute of Technology OWCh),

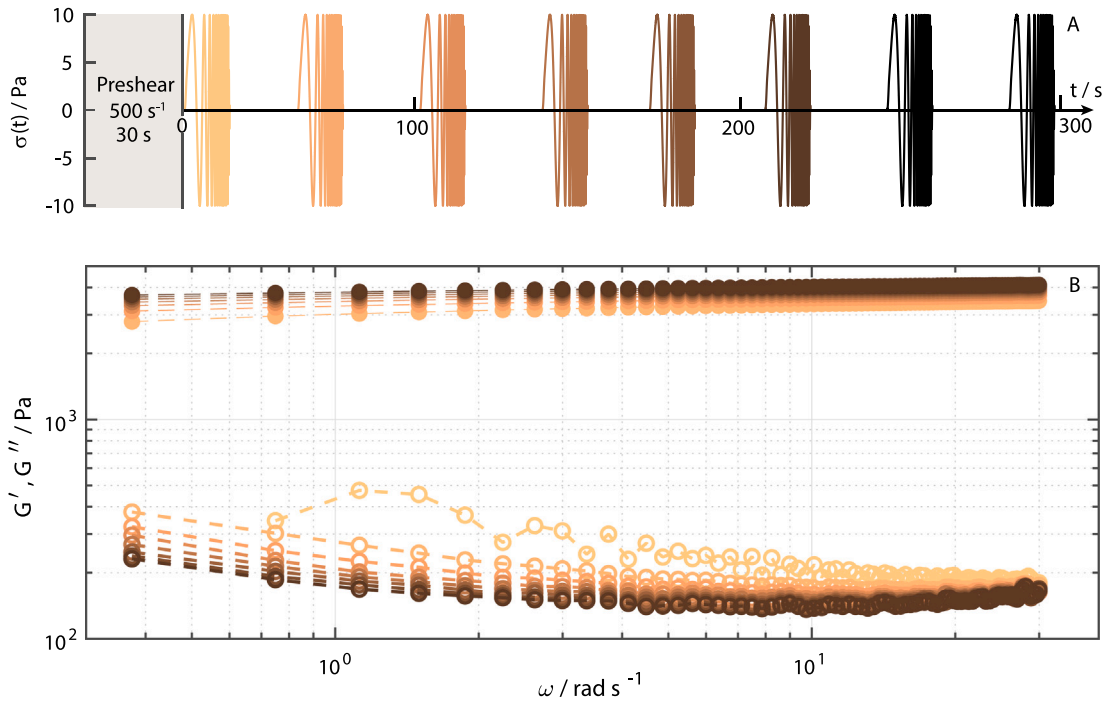

Fig. 16. Evolution of the time- and frequency-dependent linear viscoelastic moduli (i.e. the storage modulus $G'(\omega, t)$, represented by filled circles and the loss modulus $G''(\omega, t)$, represented by hollow circles) as measured using a repeated sequence of eight stress -controlled chirps of length $\Delta T = 14$ s conducted immediately after preshearing (letherization) of the sample for $t = 30$ s is ceased. The colour of the symbols for the elastic and viscous moduli vary from light orange to black to represent the evolving sample age, t_w.

which is available as an executable file that may be installed alongside, and integrated within the workflow of TA Instrument's TRIOS, and/or Anton Paar's RheoCompass rheometer control software. The software is available via email to the authors at sumit-owch@swansea.ac.uk.

4.2. Strain controlled chirp rheometry using CMT rheometers

Modern single-head rheometers are generally capable of operating in both stress-controlled mode (in which the torque applied to the sample is directly controlled) and in a strain-controlled mode (in which rapid instrument-specific feedback loops are used to achieve the desired command strain waveform). Whilst these feedback loops are optimised for viscometric and conventional SAOS experiments in certain cases, they can also be successfully employed when performing chirp-based experiments thus avoiding the offset issue noted above. However, waveform design and subsequent analysis remain subject to the limitations associated with LUT size and instrument inertia. SUMIT OWCh can be used to design/analyse both stress-controlled and strain-controlled experiments performed using single-head rheometers. However, it is important to note that the actual strain waveform that is applied to the sample and the command chirp may differ significantly as a result of the internal instrument feedback loops and caution must be exercised when using this operating mode.

CRediT authorship contribution statement

Rebecca E. Hudson-Kershaw: Writing – review & editing, Writing – original draft, Methodology, Investigation, Formal analysis. **Mohua Das:** Writing – review & editing, Writing – original draft, Validation, Investigation. **Gareth H. McKinley:** Writing – review & editing, Supervision, Methodology. **Daniel J. Curtis:** Writing – review & editing, Writing – original draft, Visualization, Validation, Supervision, Project administration, Methodology, Investigation, Funding acquisition, Formal analysis, Conceptualization.

Declaration of competing interest

The authors declare the following financial interests/personal relationships which may be considered as potential competing interests: Daniel J. Curtis reports financial support was provided by Engineering and Physical Sciences Research Council. Daniel J. Curtis reports financial support was provided by Welsh Government. Daniel J. Curtis is serving as a Guest Editor for the Special Issue of JNNFM to which this article is being submitted. Gareth H. McKinley serves on the Editorial Board of JNNFM. The journal's Editors-in-Chief will process and make decisions regarding the manuscript. Gareth H. McKinley & Mohua Das were supported, in part, by a gift from the Procter & Gamble Corporation. If there are other authors, they declare that they have no known competing financial interests or personal relationships that could have appeared to influence the work reported in this paper.

Data availability

Data will be made available on request.

Acknowledgements

The authors acknowledge funding from the Engineering and Physical Sciences Research Council, UK through grants EP/N013506/1 (DJC) & EP/T026154/1 (DJC, REH) and the Welsh Government (DJC) via SmartExpertise and Capital Equipment programmes.

Appendix A. Supplementary data

Supplementary material related to this article can be found online at https://doi.org/10.1016/j.jnnfm.2024.105307.

References

[1] H.H. Winter, F. Chambon, Analysis of linear viscoelasticity of a crosslinking polymer at the gel point, J. Rheol. 30 (1986) 367–382.

[2] F. Chambon, H.H. Winter, Linear viscoelasticity at the gel point of a crosslinking PDMS with imbalanced stoichiometry, J. Rheol. 31 (1987) 683–697.

[3] A.J. Holder, N. Badiei, K. Hawkins, C. Wright, P.R. Williams, D.J. Curtis, Control of collagen gel mechanical properties through manipulation of gelation conditions near the sol–gel transition, Soft Matter 14 (2018) 575–580.

[4] K. Hawkins, P.A. Evans, M. Lawrence, D. Curtis, M. Davies, P.R. Williams, The development of rheometry for strain-sensitive gelling systems and its application in a study of fibrin–thrombin gel formation, Rheol. Acta 49 (2010) 891–900.

[5] E.E. Holly, S.K. Venkataraman, F. Chambon, H.H. Winter, Fourier transform mechanical spectroscopy of viscoelastic materials with transient structure, J. Non-Newton. Fluid Mech. 27 (1988) 17–26.

[6] K. Hawkins, M. Lawrence, P.W. Williams, R.L. Williams, A study of gelatin gelation by Fourier transform mechanical spectroscopy, J. Non-Newton. Fluid Mech. 148 (1) (2008) 127–133.

[7] M. Geri, B. Keshavarz, T. Divoux, C. Clasen, D.J. Curtis, G.H. McKinley, Time-resolved mechanical spectroscopy of soft materials via optimally windowed chirps, Phys. Rev. X 8 (2018) 041042.

[8] M. Tassieri, M. Laurati, D.J. Curtis, D.W. Auhl, S. Coppola, A. Scalfati, K. Hawkins, P.R. Williams, J.M. Cooper, i-Rheo: Measuring the materials' linear viscoelastic properties "in a step"!, Journal of Rheology 60 (4) (2016) 649–660.

[9] W. Hardiman, M. Clark, C. Friel, A. Huett, F. Pérez-Cota, K. Setchfield, A.J. Wright, M. Tassieri, Living cells as a biological analog of optical tweezers – a non-invasive microrheology approach, Acta Biomaterialia (ISSN: 1742-7061) 166 (2023) 317–325.

[10] J. Ramírez, G.M. Gibson, M. Tassieri, Optical halo: A proof of concept for a new broadband microrheology tool, Micromachines 15 (7) (2024).

[11] R. Ferraro, S. Guido, S. Caserta, M. Tassieri, i-Rheo-optical assay: Measuring the viscoelastic properties of multicellular spheroids, Mater Today Bio. 26 (2024) 101066.

[12] E. Ghiringhelli, D. Roux, D. Bleses, H. Galliard, F. Caton, Optimal Fourier rheometry, Rheol. Acta 51 (2012) 413–420.

[13] J. Rouyer, A. Poulesquen, Evidecnce of a fractal percolating network during geopolymerisation, J. Am. Ceram. Soc. 98 (2015) 1580–1587.

[14] D.J. Curtis, A. Holder, N. Badiei, J. Claypole, M. Walters, B. Thomas, M. Barrow, D. Deganello, M.R. Brown, P.R. Williams, K. Hawkins, Validation of optimal Fourier rheometry for rapidly gelling materials and its application in the study of collagen gelation, J. Non-Newton. Fluid Mech. 222 (2015) 253–259.

[15] T. Athanasiou, M. Geri, P. Roose, G.H. McKinley, G. Petekidis, High-frequency optimally windowed chirp rheometry for rapidly evolving viscoelastic materials: Application to a crosslinking thermoset, J. Rheol. 68 (2024) 445–462.

[16] P. Fausti, A. Farina, Acoustic measurements in opera houses: Comparison between different techniques and equipment, J. Sound Vib. 232 (2000) 213–229.

[17] J. Klauder, A.C. Price, S. Darlington, W.J. Albersheim, The theory and design of chirp radars, Bell Syst. Tech. J. 39 (1960) 745–808.

[18] B. Keshavarz, D.G. Rodrigues, J.B. Champenois, M.G. Frith, J. Ilavsky, M. Geri, T. Divoux, G.H. McKinley, A. Poulesquen, Time–connectivity superposition and the gel/glass duality of weak colloidal gels, Proc. Natl. Acad. Sci. 118 (15) (2021).

[19] J.D.J. Rathinaraj, J. Hendricks, C. Clasen, G.H. McKinley, OrthoChirp: A fast spectro-mechanical probe for monitoring transient microstructural evolution of complex fluids during shear, J. Non-Newton. Fluid Mech. 301 (2022) 104744.

[20] J.D.J. Rathinaraj, K.R. Lennon, M. Gonzalez, A. Santra, J.W. Swan, G.H. McKinley, Elastoviscoplasticity, hyperaging, and time–age-time–temperature superposition in aqueous dispersions of bentonite clay, Soft Matter 19 (2023) 7293–7312.

[21] J. Lauger, H. Stettin, Differences between stress and strain control in the non-linear behavior of complex fluids, Rheol. Acta 49 (2010) 909–930.

[22] J.C. Lee, Y.T. Hong, K.M. Weigandt, E.G. Kelly, H. Kong, S.A. Rogers, Strain shifts under stress-controlled oscillatory shearing in theoretical, experimental, and structural perspectives: Application to probing zero-shear viscosity, J. Rheol. 63 (2019) 863–881.

[23] O. Hassager, Stress-controlled oscillatory flow initiated at time zero: A linear viscoelastic anlaysis, J. Rheol. 64 (2020) 545–550.

[24] A. Ogunkeye, R. Hudson, D.J. Curtis, The effect of instrument inertia on the initiation of oscillatory flow in stress controlled rheometry, J. Rheol. 67 (2023) 1175–1187.

[25] R.H. Ewoldt, M.T. Johnston, L.M. Caretta, Experimental challenges of shear rheology: how to avoid bad data, in: S. Spagnolie (Ed.), Complex Fluids in Biological Systems, Springer, 2015.

[26] J. Lauger, H. Stettin, Effects of instrument and fluid inertia in oscillatory shear in rotational rheometers, J. Rheol. 60 (2016) 393–406.

[27] R.H. Ewoldt, G.H. McKinley, Creep ringing in rheometry, Rheol. Bull. 76 (2007) 4–24.

[28] C. Baravian, D. Quemada, Using instrumental inertia in controlled stress rheometry, Rheol. Acta 37 (1998) 223–233.

[29] C. Baravian, G. Benbelkacem, F. Caton, Unsteady rheometry: can we characterize weak gels with a controlled stress rheometer? Rheol. Acta 46 (2006) 577–581.

[30] I. Krieger, The role of instrument inertia in controlled stress rheometers, J. Rheol. 34 (1990) 471–483.

[31] R.E. Hudson, A.J. Holder, K.M. Hawkins, P.R. Williams, D.J. Curtis, An enhanced rheometer inertia correction procedure (ERIC) for the study of gelling systems using combined motor-transducer rheometers, Phys. Fluids 29 (2017) 121602.

[32] K. Walters, Rheometry, Chapman and Hall, ISBN: 9780470919262, 1975.

[33] N.W. Tschoegl, The Phenomenological Theory of Linear Viscoelastic Behaviour, Springer-Verlag, Berlin, 1989.

[34] J.L. Schrag, Deviation of velocity gradient profiles from the "gap loading" and "surface loading" limits in dynamic simple shear experiments, Trans. Soc. Rheol. 21 (1977) 399–413.

[35] T.A. Instruments, Rheology Theory and Applications, Technical Report, TA Instruments, 2016.

[36] The MathWorks Inc., Matlab (r2023b), 2023.

[37] H. Nyquist, Certain topics in telegraph transmission theory, Trans. Am. Inst. Electr. Eng. 47 (2) (1928) 617–644.

[38] A.V. Oppenheim, A.S. Willsky, S.H. Nawab, Signals & Systems, in: Prentice-Hall Signal Processing Series, Prentice-Hall International, ISBN: 9780136511755, 1997.

[39] K.W. Ebagninin, A. Benchabane, K. Bekkour, Rheological characterization of poly (ethylene oxide) solutions of different molecular weights, J. Colloid Interface Sci. 336 (1) (2009) 360–367.

[40] Y.T. Hu, A. Lips, Kinetics and mechanism of shear banding in an entangled micellar solution, J. Rheol. 49 (2005) 1001–1047.

[41] Y.T. Hu, C. Palla, A. Lips, Comparison between shear banding and shear thinning in entangled micellar solutions, J. Rheol. 52 (2008) 279.

[42] P. Cheng, M.C. Burroughs, G.L. Leal, M.E. Helgeson, Distinguishing shear banding from shear thinning in flows with a shear stress gradient, Rheol. Acta 56 (2017) 1007–1032.

[43] H.H. Winter, P. Morganelli, F. Chambon, Stoichiometry effects on rheology of model polyurethanes at the gel point, Macromolecules 21 (1988) 532–535.

[44] M. Mours, H.H. Winter, Time-resolved rheometry, Rheol. Acta 33 (1994) 385–397.

[45] M. Pilavtepe, S.M. Recktenwald, R. Schuhmann, K. Emmerich, N. Willenbacher, Macro-and microscale structure formation and aging in different arrested states of laponite dispersions, J. Rheol. 62 (2) (2018) 593–605.

[46] A. Shukla, S. Shanbhag, Y.M. Joshi, Analysis of linear viscoelasticity of aging soft glasses, J. Rheol. 64 (5) (2020) 1197–1207.